

GRENOBLE-INP PHELMA

NANOTECHNOLOGIES FOR ICTS

Development and characterization of a Giant Magneto-Impedance current sensor

Supervisor :

HOUIS Simon
Shu@melexis.com

ASF4UR Aktham
Aktham.Asfour@g2elab.grenoble-inp.fr

Student :

PERQUE Jérémie
Jeremie.Perque@grenoble-inp.org

TUTOR: PREJBEANU Liliana
Liliana.buda@cea.fr



Switzerland: Chem. de Buchaux 38, 2022 Bevoir

February 13th - August 4

Master thesis: 2023

Acknowledgments

I would like to express my sincere gratitude to the G2ELAB team, starting with Aktham ASFOUR, who guided me throughout the first month of this internship, imparting invaluable knowledge and advice, and showing exceptional kindness towards me.

I am grateful to Simon HOUIS for supervising me during my time in Switzerland. I would also like to thank the rest of the Innovation team, including Dirk ETTELT, Eugene LOMAKIN, and others, for always being available to answer my questions and offer assistance.

I also want to acknowledge the valuable assistance I received from Alain BUCHAILLARD during my spice simulation period, as well as the continuous support provided by Hugues DEBIEUX in the lab.

I would also like to thank the other interns especially Arthur NICOLA, Baptiste FREMENT, Nicolas AU-DOIN and Jan-Philipp KODDENBERG for filling these 6 months with unforgettable moments.

Lastly, I want to express my gratitude to everyone at the Melexis Bevaix site for providing me with the opportunity to undertake this internship and for their warm welcome to the company.

Abstracts

English

During my internship, my primary objective was to develop a cost-effective current sensor with advanced sensitivity using the Giant Magneto Impedance (GMI) effect. Leveraging Melexis' expertise along with state-of-the-art knowledge, I designed a GMI sensor incorporating key blocks such as excitation, demodulation, and amplification with offset correction. I conducted a comprehensive simulation of the sensor using LTspice, enabling me to anticipate its behavior and refine its design for improved performance. I selected a commercial vitrovac ribbon transducer as the sensing element due to its impedance variation characteristics. Additionally, I applied magnetic biasing to maintain linearity around a zero magnetic field. Subsequently, I characterized the sensor using a Helmholtz coil setup to validate its operational principle. Finally, I conducted applicative tests using a current generator to evaluate the sensor's linearity and signal-to-noise ratio, ultimately validating the final operation of the current sensor.

Français

Au cours de mon stage, mon objectif principal a été de développer un capteur de courant peu coûteux doté d'une grande sensibilité en exploitant l'effet Magnéto Impédant Géant (GMI). En utilisant l'expertise de Melexis ainsi que l'état de l'art, j'ai conçu un capteur GMI comprenant des blocs clés tels que l'excitation, la démodulation et l'amplification avec correction d'offset. J'ai réalisé la simulation complète du capteur à l'aide de LTspice, ce qui m'a permis d'anticiper son comportement et d'affiner sa conception pour obtenir de meilleures performances. J'ai choisi un ruban commercial en vitrovac comme élément sensible en raison de ses caractéristiques de variation d'impédance. De plus, j'ai appliqué une polarisation magnétique pour maintenir la linéarité autour d'un champ magnétique nul. Ensuite, j'ai caractérisé le capteur en utilisant un banc de test constitué de bobines d'Helmholtz afin de valider son principe opérationnel. Enfin, j'ai réalisé des tests applicatifs à l'aide d'un générateur de courant pour évaluer la linéarité et le rapport signal/bruit du capteur, validant ainsi le fonctionnement final du capteur de courant.

Italiano

Durante il mio stage, il mio obiettivo principale era sviluppare un sensore di corrente a basso costo con sensibilità avanzata sfruttando l'effetto dell'Impedenza Magnetica Gigante (GMI). Sfruttando l'esperienza di Melexis insieme alla conoscenza dello stato dell'arte, ho progettato un sensore GMI che comprendeva blocchi chiave come l'escitazione, la demodulazione e l'amplificazione con correzione dell'offset. Ho condotto una simulazione completa del sensore utilizzando LTspice, permettendomi di anticiparne il comportamento e affinare il suo design per ottenere prestazioni migliorate. Ho selezionato un trasduttore a nastro vitrovac commerciale come elemento sensibile a causa delle sue caratteristiche di variazione di impedenza. Inoltre, ho applicato una polarizzazione magnetica per mantenere la linearità intorno a un campo magnetico nullo. Successivamente, ho caratterizzato il sensore utilizzando una configurazione di bobina di Helmholtz per convalidare il principio operativo. Infine, ho condotto test applicativi utilizzando un generatore di corrente per valutare la linearità e il rapporto segnale/rumore del sensore, convalidando in definitiva il funzionamento finale del sensore di corrente.

Contents

1	Introduction	1
1.1	About G2ELAB	1
1.2	About Melexis	1
1.3	Internship progress	1
2	Giant Magneto-Impedance review	3
2.1	Origin and principle of the GMI effect	3
2.1.1	GMI effect	3
2.1.2	Frequency regimes	4
2.1.2.1	Low frequency regime 1 kHz - 100 kHz	4
2.1.2.2	The intermediate or high-frequency regime 100 kHz - 100 MHz	4
2.1.2.3	The very high-frequency regime 100 MHz - a few GHz	4
2.1.3	Impedance characteristic	5
2.1.3.1	Non linearity of the curve	5
2.1.3.2	Biasing solution	6
3	GMI sensor	6
3.1	GMI in the state of the art	6
3.2	Melexis target specification	6
3.3	Sensor Block Diagram	7
3.3.1	Sensitive element	8
3.3.2	Excitation system	9
3.3.2.1	Independent GMI oscillator	10
3.3.2.2	Integrated GMI oscillator	11
3.3.3	Demodulation system	11
3.3.4	Amplification system	13
3.3.5	Chosen sensor topology	14
4	Simulation	14
4.1	Single GMI sensor	14
4.1.1	Excitation system	15
4.1.1.1	RC astable multivibrator	15
4.1.1.2	Pulse width modulation	16
4.1.1.3	Buffer and injection resistance	17
4.1.2	Sensitive Element	18
4.1.3	Demodulation	18
4.1.3.1	Limiting amplification for demodulation	19
4.1.3.2	Low pass filter	19
4.1.4	Offset correction	20
4.1.5	Simulation of calibration	21
4.1.6	Performance and noise	23
4.2	Dual GMI sensor	24
4.2.1	Dual RC Astable oscillator	25
4.2.2	Performance and estimated noise	26
5	PCB design	28
5.1	GMI holder	28
5.2	Electronics	30
5.3	PCB result	31

6	Characterization	32
6.1	3D Support and characterization of the biasing coil	32
6.2	Impedance characterization setup and first functioning result	33
6.3	First sensor result using the Figure 43 setup	34
6.3.1	1 GMI configuration	34
6.3.2	2 GMI configuration	34
6.4	Impedance characteristics for different configuration	35
6.4.1	Duty cycle variation	35
6.4.1.1	1 GMI configuration	35
6.4.1.2	2 GMI configuration	35
6.4.2	Gain shift variation	36
6.4.2.1	1 GMI configuration	36
6.4.2.2	2 GMI configuration	36
6.5	Applicative test result using a kepcos current supply	37
6.5.1	1 GMI configuration	38
6.5.2	2 GMI configuration	39
6.6	Addressing drawbacks and exploring sensor amelioration	40
6.6.1	Bandwidth	40
6.6.2	Noise	41
6.6.3	Some limitations	42
7	Conclusion	43
8	ANNEX	44
8.1	List of figures	44
8.2	References	45
8.3	Quick explanation of the measurement setup	46
8.4	Voltage control oscillator	47
8.5	Complementary figures and tables	49

1 Introduction

This internship aims at developing and characterizing a demonstrator **Giant Magneto-Impedance** (GMI) based current sensor. The internship was conducted in collaboration between two sites and happened 25% of the time at the **G2ELAB** laboratory in Grenoble and 75% at **Melexis Bevaix** (Figure 1).

1.1 About G2ELAB

During my time in Grenoble, I had the privilege of working under the guidance of Aktham Asfour, a teacher-researcher and member of the MADEA team (Materials, Machines and Advanced Electromagnetic Devices) at G2ELAB. This team is renowned for its interdisciplinary approach towards developing innovative systems, with a focus on understanding materials, electrical engineering, and electromagnetic structure calculations. Their research revolves around four main themes: functional materials for electrical engineering, system design and modeling, innovative energy conversion and processing devices, and energy management devices. The MADEA team has gained significant expertise in this field by utilizing specialized material characterization and machine testing equipment, as well as by producing tangible demonstrators and software¹.

1.2 About Melexis

I continued at Melexis Bevaix where I was part of the innovation team for the remaining 4.5 month of the internship. Melexis is a global supplier of micro-electronic semiconductor. They offer a wide range of semiconductor integrated circuits that cover various sensor technologies, drivers, and transceivers. Their main application areas are automotive, power train electrification, and E-mobility. The sensors they commercialize include current sensor ICs based on hall effect technology, magnetic position sensors for ICs, and tri-axis hall-based position sensors. These sensors are utilized to power various applications in the industries they serve, such as electric bike motors, onboard chargers for electric vehicles, and internal combustion engine (ICE) gasoline management and treatment systems².



(a) G2ELAB site



(b) Melexis Bevaix site

Figure 1: Internship locations

1.3 Internship progress

The internship focused on developing a current sensor readout circuitry using the Melexis sensitive element based on Giant Magneto Impedance (GMI). The primary objective was to understand the GMI phenomena

¹<https://g2elab.grenoble-inp.fr/en/research/madea>

²<https://www.melexis.com/en>

by conducting a comprehensive review of the current state-of-the-art in GMI current sensor technology and other current sensor technologies.

To achieve this, a comparison of GMI sensor readout circuits was carried out at G2elab. Essential block diagrams and schematics were then established, taking into consideration PCB integration and overall performance requirements. The selected electrical circuit was further simulated using Ltspice to gain a deeper understanding of its behavior.

Subsequently, the sensor was designed on a PCB using Altium and fully assembled. To validate its performance, the sensor underwent characterization using the Melexis Helmholtz setup. This involved testing and evaluating its sensitivity and other relevant parameters.

The project aimed to leverage Melexis’ 20-year expertise in CMOS ferromagnetic layer deposition (MFI) to propose low-cost current sensors with exceptional sensitivity based on GMI technology.

Here is the global estimated work package for this internship ((Figure 2).

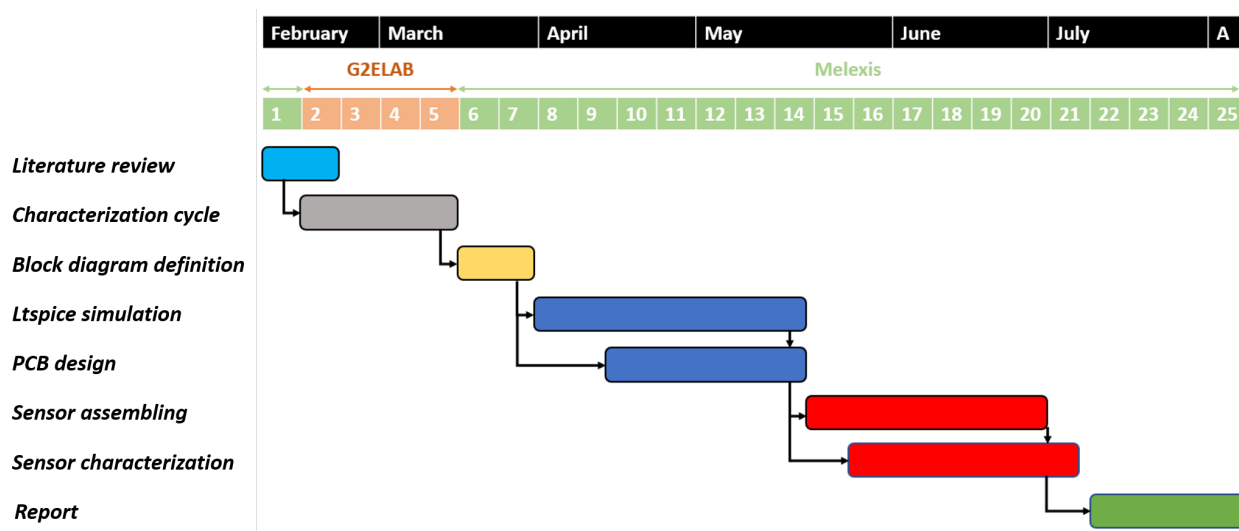


Figure 2: Estimated Gantt chart

At the end of this report, we will briefly compare the real project timeline and task dependencies with those presented in Figure 2.

2 Giant Magneto-Impedance review

The introductory chapter of this thesis aims to provide a comprehensive understanding of the giant magneto impedance effect, its underlying principles, and its implications for the design and performance of current sensors.

2.1 Origin and principle of the GMI effect

The discovery of the magneto-impedance effect traces back to Harrison's research on Nickel wire in the 1930s (see [1]). However, it was not until the end of the 20th century, specifically with the work of K. Mohri and Panina (see [2]), that the GMI effect was first published and experimental sensor designs utilizing this technology were introduced. GMI refers to the **variation of the real and imaginary part of the impedance** observed in soft magnetic materials, typically ribbons or wires, when subjected to an external magnetic field while an alternating current passes through the conductor (see [3]). Despite being relatively nascent, this technology exhibits significant potential for magnetic and current sensor applications due to its cost-effectiveness, simple design, and high sensitivity. Moreover, the broad measurement bandwidth of these sensors could potentially enable Melexis to expand into other economic sectors, such as the medical field.

2.1.1 GMI effect

The change of impedance is induced by the permeability-dependent variation of skin depth $\delta = \sqrt{\frac{2}{\sigma * \omega * \mu(H)}}$ when an AC current is flowing through the conductor. The typical configuration for the GMI cylindrical sample micro wire is the following:

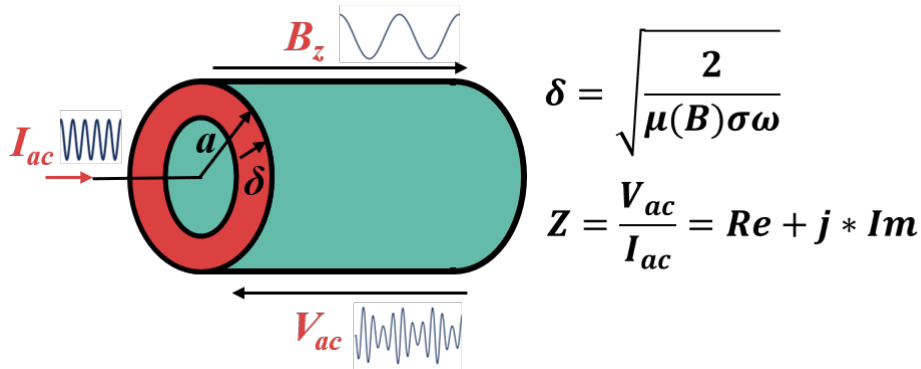


Figure 3: GMI representation for a wire sample with the typical physical quantities involved

As highlighted by this figure the GMI effect relies on understanding the interconnections between the electric and magnetic fields at the surface of the sample as well as the magnetization mechanisms within the material, which involve domain wall movements and magnetization rotation within the material. Indeed, as the magnetic field increases along the z-axis, it alters the magnetic permeability μ of the sample, subsequently influencing the skin depth δ . This variation in skin depth leads to a corresponding change in impedance, as the current now flows through a reduced surface area within the sample. The GMI impedance is a complex quantity define as $\underline{Z} = \frac{V_{ac}}{I_{ac}}$ which depends off the frequency f of the alternative current $\underline{I_{ac}} = I_{ac} * e^{-j2\pi ft}$. The variation of the real and imaginary parts of the impedance, as well as the detectable range of magnetic fields, depend on the frequency at which we operate the alternating current supply. Later on, it will be evident that the detectable magnetic field could reach up to frequencies equal to one-tenth of the current frequency. This is mainly to ensure compliance with the cutoff frequency of the low pass filter when designing the demodulation block that will compose the future current sensor. In the following paragraph, we will provide a concise overview of the various frequency regimes that our sample may encounter.

2.1.2 Frequency regimes

In case of the GMI there are mainly 3 different frequency regimes that the sample could encounter (see [4]). In order to have a better understanding, here is a quick illustration of the skin effect represented by the current density for different frequencies:

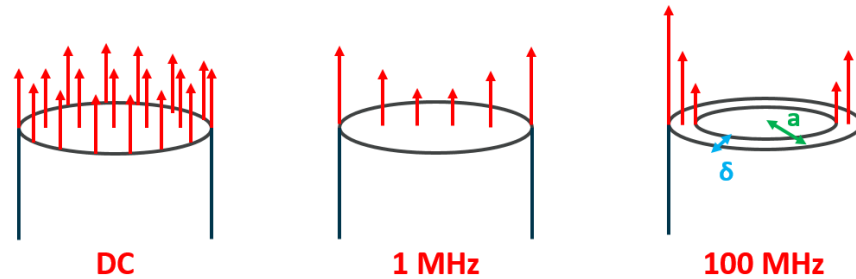


Figure 4: Skin effect: Current density at different frequencies through a wire

2.1.2.1 Low frequency regime 1 kHz - 100 kHz

In this operating regime, the variation of magnetic permeability causes a skin effect. But since the value of the excitation frequency of the sensitive element is low, we have ($\delta \gg a$). As a result, the real part of the impedance, which represents the resistive component of the impedance, remains unchanged. However, the change in permeability still affects the imaginary part of the impedance, corresponding to the inductive component. A typical formula which represent the inductance of a soft magnetic wire is $L = \frac{\mu\Phi l}{2}$ where $\mu\Phi$ is the circumferential permeability linked to the circumferential field $h\Phi$ and l is the length of the wire.

Finally in this regime the impedance expression can be approximated as follow $\underline{Z} = Rdc + j * h(Hz, Iac, f)$. Here, we are referring to the phenomenon of **self-induction** since only the imaginary part is varying.

2.1.2.2 The intermediate or high-frequency regime 100 kHz - 100 MHz

In this regime, both the real and imaginary components of the impedance vary with the applied magnetic field. This effect is associated with the occurrence of the skin effect in the conductor due to the increase of frequency of the alternative current ($\delta \ll a$). The skin depth, which determines the concentration of current distribution within the material, is related to the magnetic permeability, which in turn varies with the applied magnetic field.

The impedance expression is approximated as follows $\underline{Z} = g(Hz, Iac, f) + j * k(Hz, Iac, f)$. Here, we are referring to the phenomenon of **Giant magneto-impedance** since both the real and imaginary part are varying.

2.1.2.3 The very high-frequency regime 100 MHz - a few GHz

As the frequency increases, it becomes increasingly challenging to ascertain the impedance variation and formula due to the relationship between the magnetic permeability and the attainment of conditions for ferromagnetic resonance (FMR) accompanied by material saturation.

For the remainder of this project, we will consider the intermediate frequency regime in all cases.

2.1.3 Impedance characteristic

To optimize the variation in impedance, careful consideration needs to be given to various factors such as geometry, composition, fabrication method, material softness and magnetic anisotropy. Achieving the desired impedance variation entails selecting materials with specific characteristics, including low magnetostriction, significant saturation magnetization, and high permeability. These properties play a crucial role in enhancing the GMI phenomenon.

Now, let's expose into the typical characteristic curve of GMI impedance, which illustrates the relationship between impedance and the applied magnetic field

2.1.3.1 Non linearity of the curve

The characteristics curves of GMI displays non linearity impedance curve, without distinguishing between positive and negative magnetic external fields. As our internship revolves around **ruban shape GMI**, we will illustrate the impedance characteristic of these shapes in [Figure 5](#). These disparities can be explained and experimentally observed by the orientation of the magnetic anisotropy of the sample. Additionally, it is worth noting that other GMI configurations using additional coil, such as the off-diagonal configuration, exhibit different impedance curves which are more linear around zero field. However, for the scope of this report, we will not present these specific configurations. In the next figure the red rectangle represent the soft magnetic material, H_A the magnetic anisotropy and H_{ext} the external applied field.

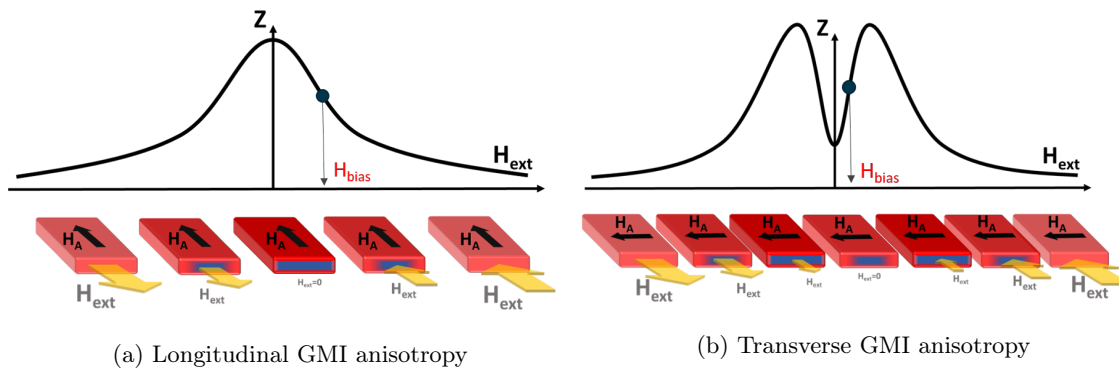


Figure 5: General impedance characteristic

Ensuring linearity around zero field is vital for sensor design. This requires careful selection of an appropriate operating point within the quasi-linear region, where maximum sensitivity is achieved. Referred to as H_{bias} , this operating point allows operate within the linear range of the impedance curve. Applying a bias magnetic field to the sample enables to position the operating point in the linear regime. Essentially, this corresponds to a leftward shift of the curve.

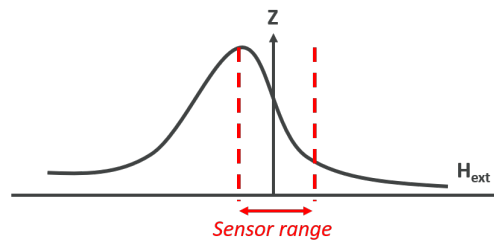


Figure 6: Example of a biased curve for a longitudinal GMI anisotropy

2.1.3.2 Biasing solution

The issue with the biasing method of Figure 5 is that it leads to an intrinsic offset at zero magnetic field which will be reported in the voltage output of the sensor. Additionally, this intrinsic offset could also be influenced by various parameters such as temperature and stress. To address this issue, several solutions could be implemented. One of them would be to directly suppress the offset by subtracting the zero-field impedance value using a differential amplifier in the readout circuitry. The biasing issue could potentially be resolved through alternative biasing or employing two different GMI samples with opposing biases. Here is the illustrated impedance curve of the subtraction of two GMI curve with opposite biasing:

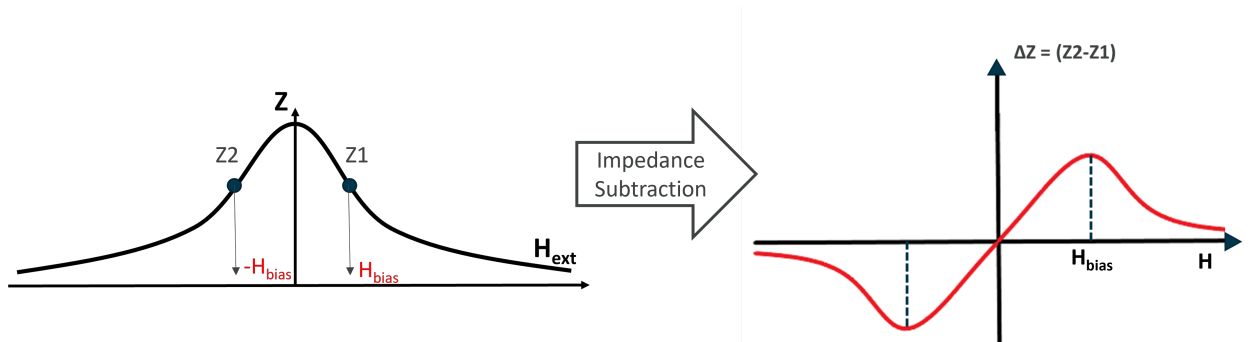


Figure 7: Differential transducer characteristic for a longitudinal impedance curve

In the design of the sensor we will be using two different techniques to suppress the offset, directly suppressing the offset with a DC voltage control and subtracting two GMI output.

3 GMI sensor

In the following chapter, we will explore the various block diagrams that constitute the sensor and goes into the rationale behind our selection process for the different block. Furthermore, we will conduct a brief comparison between the performance of the existing magnetic current sensor and the target specifications of the Melexis GMI sensor.

3.1 GMI in the state of the art

GMI-based sensors could revolutionize magnetic field measurements by offering several advantages over traditional sensors. Indeed, unlike traditional fluxgate sensors with a limited measurement bandwidth of approximately 100 kHz (see [5]), GMI-based sensors offer a significantly enhanced bandwidth, enabling the accurate measurement of both direct current (DC) and alternating current (AC) magnetic fields. Furthermore, the GMI sensor exhibits superior sensitivity compared to the conventional Hall effect sensor, with a sensitivity of 1mV/mT. This heightened sensitivity allows magnetic field measurements across a wide range of applications. Additionally, unlike other methods such as Rogowski coils and current transformers, the GMI sensor's versatility extends beyond AC measurements, facilitating the measurement of both DC and AC currents. These features make GMI-based sensors an ideal choice for a wide range of applications, offering improved performance and expanded capabilities in magnetic field sensing. Notice that there are many other sensor in the state of the art such as magnetoresistif sensor family and SQUID but their working principle will not be explain in this report, for further information please refer to [3].

3.2 Melexis target specification

In line with the initial stage of technology readiness, specifically TRL1, the GMI team has formulated specific target specifications for the internship project that we aim to achieve

Requirements	Target Specifications			Rationale
	Min	Typ	Max	
Primary measurement function				
Gradiometric concept		Yes		Aligned on customers' roadmap regarding the coreless technology
Current budget for the sensor: coil(s)+GMI transducer(s)		10mA		Considering max 20mA of chip supply current. 10mA remaining for readout circuitry.
Magnetic anisotropy		Yes/No		Without annealing, the GMI elements display naturally a longitudinal anisotropy (shape anisotropy)
Sensor Output Linearity		0.5%FS		Gen3 spec for fast analog current sensor
Noise Free bits, BW = 500Hz	12.5			Targeting the SNR of MLX91235GaAs stack die sensor. Same performances at lower cost since the price was a killer for MLX91235GaAs. noise calculation here.
Sensitivity [Ohm/mT]	0.122	1		Considering $\Delta x = 0.625\text{mm}$, the SNR target and the best in-class readout circuitry: MLX9037x. see 5.3.
GMI Working frequency		< 1GHz		Best frequency to be assessed regarding sensitivity and readout capability
Sensor Bandwidth		1MHz		Gen3 spec for fast analog current sensor
Working range		+/- 1.2mT		+/- 0.3 mT is considered good enough

Figure 8: Melexis target specification

The main important characteristic condition are the **bandwidth of at least 1 Megahertz** the **working range field of +/-1.2 mT** and the **sensitivity of 1Ω/mT** that we fix for the purpose of this internship.

3.3 Sensor Block Diagram

Now, let's explore the design of the GMI sensor. GMI sensors typically consist of mainly four blocks [6], often assembled as depicted in Figure 9, although variations can occur.

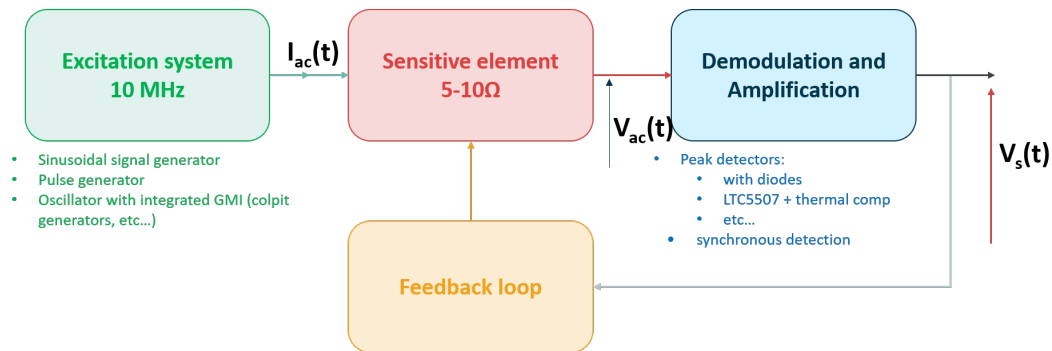


Figure 9: GMI sensor block diagram

1. The first block encompasses **the excitation system**, which supplies an alternating current of constant amplitude $I_{ac}(t)$ to the sample.

2. Next, we have **the sample** itself, which is subjected to an external magnetic field. The sample is typically made of a soft magnetic material; in this project, it will be a sample made of Vitrovac.
3. Given that the output voltage of the sample undergoes modulation due to the applied external magnetic field, a **demodulation component** becomes essential to detect the envelope of the GMI sample voltage. The envelope of the sample voltage reflects the impedance variation (Z) of the sample, as the amplitude of the alternating current remains constant.
4. Finally, we require **Amplification** and **Offset Correction**.

Lastly, there may be a feedback loop included to enhance biasing control and offset correction. However, considering the time of this internship project, **the final sensor design will not include a feedback loop**.

3.3.1 Sensitive element

In this section, we will explore the sample under consideration for this internship project. Given that the impedance variation of the IMC (Integrated Magnetic Concentrator) samples from the Melexis fab did not meet the desired requirements, the choice was made to **select an alternative sample based on Vitrovac ribbon**. This decision was aimed at validating the developed electronic circuitry.

Vitrovac is an amorphous alloy of soft magnetic material known for its exceptional properties. Unlike crystalline materials, Vitrovac lacks a regular atomic structure, which contributes to its unique magnetic behavior. When exposed to an external magnetic field, Vitrovac exhibits significant impedance variation, making it highly responsive to changes in magnetic fields. This characteristic sets it apart from the IMC sample of Melexis, as Vitrovac demonstrates superior performance in terms of impedance variation under the influence of the same magnetic fields. Vitrovac's exceptional quality makes it an invaluable option at present, as we cannot afford to wait for another batch of new wafers for this internship. By carefully cutting the sample of Vitrovac, we can achieve the desired impedance variation that is expected from the future wave of IMC sample.

We have obtained small ribbon samples from the Vitrovac 6030. Which is an amorphous alloy consisting of approximately 60% iron (Fe) and 30% nickel (Ni), with additional trace elements. This particular composition is highly regarded for its exceptional magnetic permeability and low coercivity. These properties make it ideal for applications where efficient magnetic cores or sensors are essential.

The characterization team has derived noteworthy findings (setup illustrate in annex [Figure 61](#)) from the Vitrovac 6030, creating a 3D curve that illustrates the correlation between impedance (y-axis) and external field or frequency (x-axis).

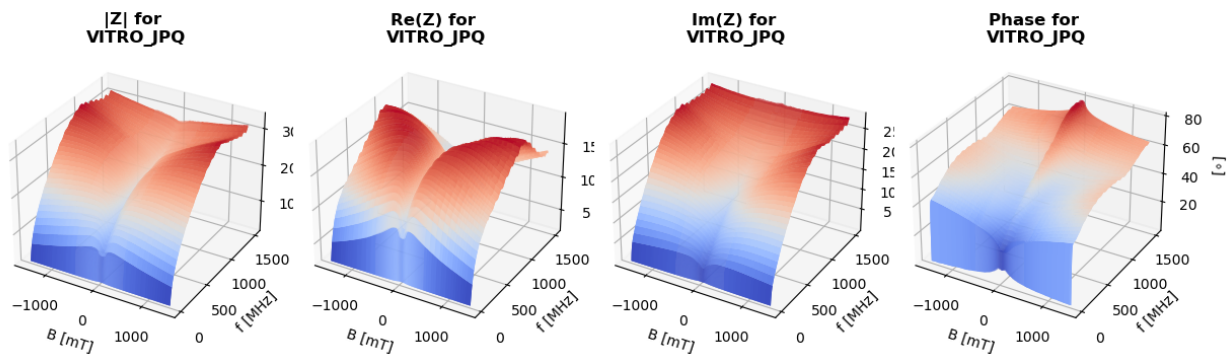


Figure 10: Impedance variation according to magnetic field and frequency

In order to effectively model the impedance sample in LTspice simulation, we made a deliberate decision to leverage the Vitrovac characteristic at a frequency of approximately 9.11 MHz. By doing so, we aim to gain valuable insights into the variation values of both the real and imaginary components of the impedance sample

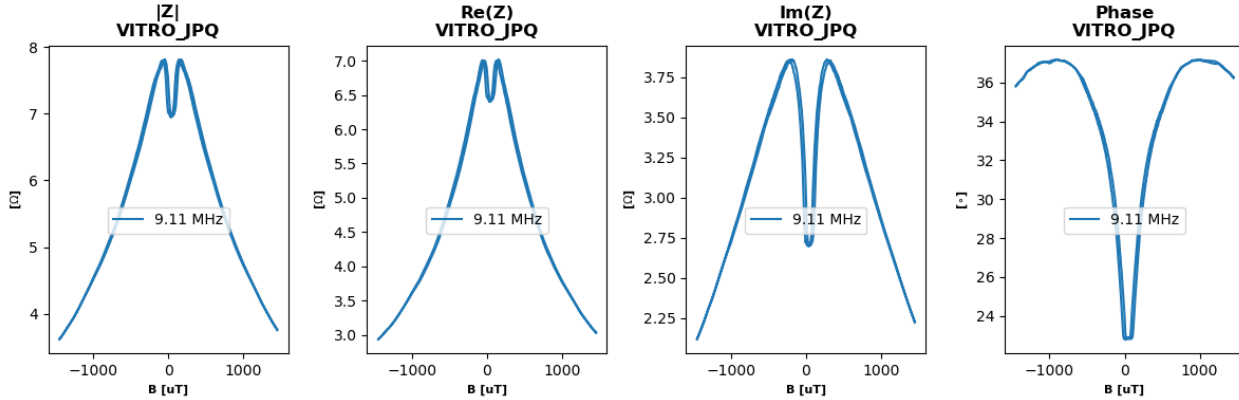


Figure 11: Vitrovac 6030 impedance curve at $F = 9.11$ MHz

Through the modeling of our GMI sample using a series combination of resistance and inductance, and assuming that the real part of impedance ($Re(z)$) is represented by R and the imaginary part ($Im(z)$) by $L2\pi f$, we can derive the maximum range of variation for R as $[3,7] \Omega$ and L as $[39,65] nH$.

3.3.2 Excitation system

After thoroughly examining the properties of the sample, we will now proceed to explore the excitation system and begin the actual design of the electrical circuitry for our GMI sensor. There are primarily two types of excitation systems: those that are independent of the GMI sample, and those that incorporate the GMI sample as an integral part of the excitation system.

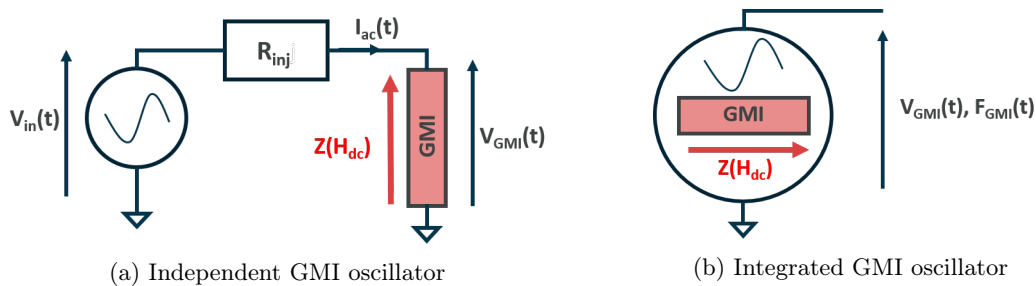


Figure 12: Block diagram of the two excitation GMI family

Figure 12 illustrates the typical block diagram of these two excitation system families. In Figure 12a, the alternating current originates from an injection resistance that converts the alternating voltage from the oscillator into a current. The output of this first excitation system family yields a voltage that is modulated by the external magnetic field. Similarly, in Figure 12b, as the GMI is integrated into the oscillator, the output voltage undergoes modulation, along with the oscillating frequency due to the GMI’s involvement in the resonant system. In this configuration, we have the flexibility to choose between voltage or frequency demodulation methods to design the next block of our sensor.

3.3.2.1 Independent GMI oscillator

In this dedicated subsection on independent oscillators, we will present several factors to consider when selecting a suitable oscillator that aligns with our planned specifications. Firstly, it is crucial to note that our oscillator should provide a **frequency of approximately 10 MHz** to ensure that the output of our GMI is modulated effectively by an external magnetic field that could go up to 1 MHz, while preventing spectral aliasing. Additionally, as we aim to design a sensor, it is important to keep the total power consumption of our circuitry as low as possible in order to accurately represent a marketable sensor. The upcoming [Figure 13](#) showcases a subset of the oscillators that have been investigated throughout this project (digital oscillator based on DDS will not be presented in this report).

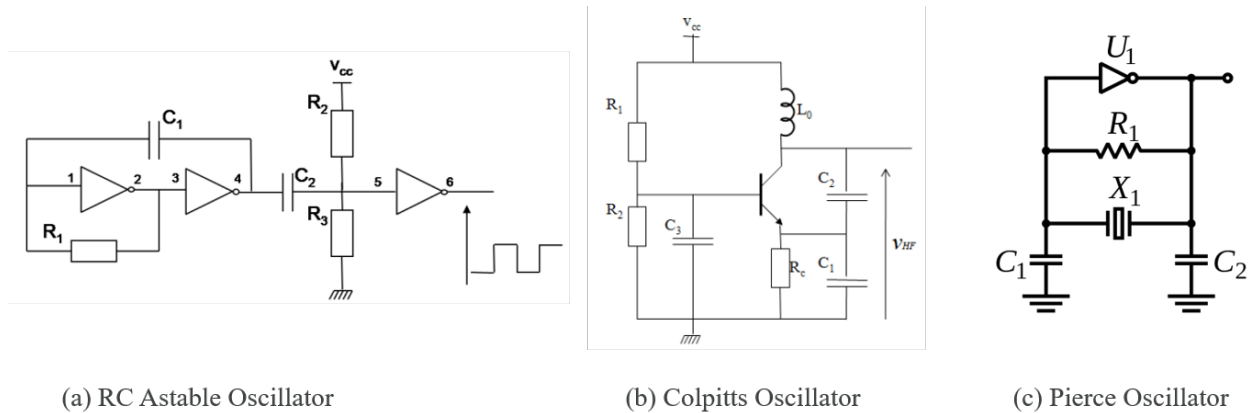


Figure 13: Exhaustive design of some oscillators

The **RC astable multivibrator** emerges as the optimal choice among these three oscillators, each based on different technologies (MOSFET, Bipolar, and quartz crystal), due to its distinctive characteristics. Unlike the others, which produce sinusoidal waveforms, the RC astable multivibrator generates pulse outputs, providing a unique advantage.

The decisive factor in selecting the RC astable multivibrator as our preferred oscillator lies in its supposedly capability to offer high sensitivity for low RMS (root mean square) input currents when employed as a pulse generator for GMI supply (see [7]). This specific feature plays a critical role in ensuring our sensor attains peak performance and accuracy.

By harnessing the power of the RC astable multivibrator, we gain access to its pulse generation capabilities, enabling us to achieve heightened sensitivity while simultaneously maintaining an efficient power consumption profile. This combination of attributes makes the RC astable multivibrator the ideal choice for our marketable sensor, empowering us to deliver a solution that excels in sensitivity, power efficiency, and real-world application requirements. It remains to be proven experimentally if it is effective.

Later in the report, we will present a more complex design of the astable oscillator and discuss its functioning principle in detail during the LTspice simulation section. This analysis aims to deepen our understanding and improve the accuracy of the simulation results.

[Figure 12a](#) illustrates the importance of designing the injection resistance to adjust the amplitude of the alternating current flowing through the GMI sample. The injection resistor serves a critical function by effectively converting voltage into current, particularly when the resistance is chosen to be larger relative to the load. This selection ensures a constant current amplitude since we have the relation $I_{ac}(t) = \frac{V_{in}(t)}{R_{inj} + Z_{gmi}(t)}$ $\approx \frac{V_{in}(t)}{R_{inj}}$ when $R_{inj} \geq Z_{gmi}(t)$. However, it is crucial to strike a suitable balance. Excessively high resis-

tance can lead to significant power dissipation within the resistor, resulting in unnecessary power loss from the oscillator. Therefore, it is essential to carefully determine the optimal value for the injection resistor, guaranteeing optimal performance and efficient power utilization. Here we could choose for example $R_{inj} = 50\Omega$ since according to Figure 11 the maximum module of the impedance should be of about 8Ω , this would guaranty a ratio of at least 5 between the 2 loads which will guarantee a constant amplitude of the current.

3.3.2.2 Integrated GMI oscillator

In this section, we will briefly discuss integrated GMI based oscillators and highlight their advantages and disadvantages compared to independent GMI based oscillators. Integrated GMI oscillators are considered clever and elegant designs because they often utilize two GMI elements within the LC resonant tank of the oscillator.

The frequency and amplitude voltage output of these oscillators are influenced by fluctuations in the external magnetic field. This characteristic can be used in applications involving frequency demodulation. By leveraging the sensitivity to external magnetic fields, these integrated GMI oscillators offer the potential for improved output performance.

Additionally, the oscillators shown in Figure 19a and 19b are based on CMOS (Complementary Metal-Oxide-Semiconductor) technology. This choice of technology offers several benefits, including integrability and compatibility with cleanroom processes. These advantages become crucial when striving to miniaturize the sensor and operate at higher frequencies, ultimately leading to an increased bandwidth of the sensor.

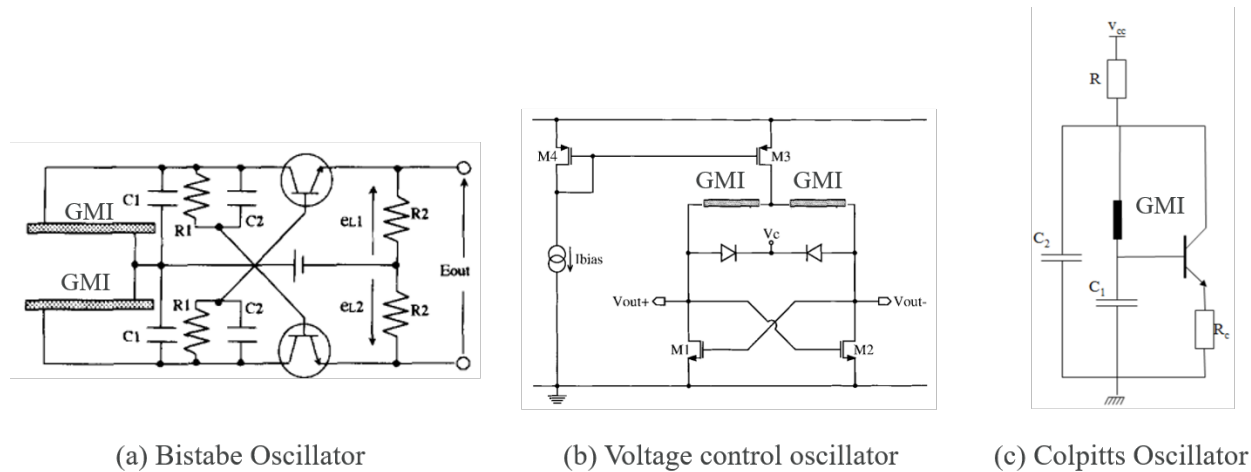


Figure 14: Design of some GMI integrated oscillators

However, controlling this technology poses challenges. In many cases, frequency control oscillators rely on variable capacitance (varicap) rather than soft magnetic materials, making it difficult to predict their behavior. Given these complexities, for the purpose of this project, we will initially adopt a simulation-based approach to model these types of oscillators.

3.3.3 Demodulation system

In this section, we will primarily focus on voltage demodulation systems, specifically AM (Amplitude Modulation). While FM (Frequency Modulation) systems are more complex to implement and only compatible with integrated GMI oscillators. Therefore, they will not be discussed in this report.

Voltage demodulation is the process of extracting the original modulating signal from a carrier wave that has been modulated with desired information. A common method for voltage demodulation is using a frequency mixer.

To understand voltage demodulation in terms of Fourier transform, consider a carrier wave modulated with a single-frequency sinusoidal signal. The modulating signal becomes embedded in the frequency spectrum of the carrier wave when it is modulated (Figure 16).

By applying a Fourier transform to the modulated signal, distinct peaks appear in the frequency spectrum. The carrier frequency manifests as a strong peak, while the modulating frequency appears as sidebands around the carrier frequency.

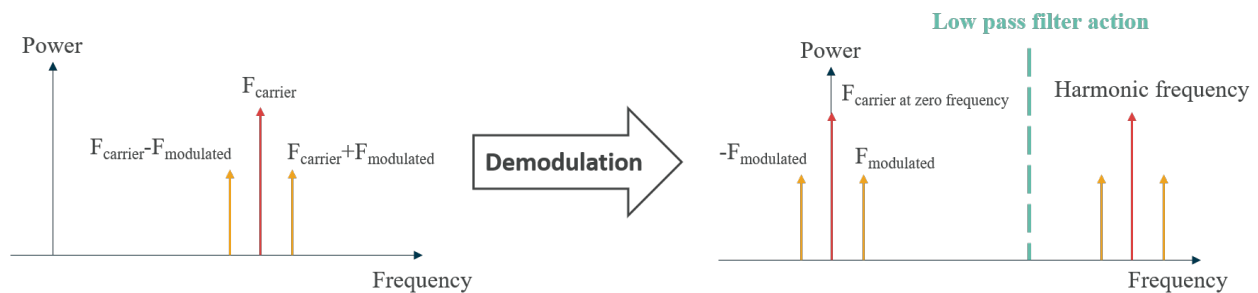


Figure 15: Amplitude demodulation explained in terms of frequency, F_{carrier} = AC current frequency, $F_{\text{modulated}}$ = External magnetic field frequency

The frequency mixer shifts the modulating signal from the carrier frequency spectrum to the base-band or lower frequency region. This facilitates the extraction of the original modulating signal, which now resides around the zero frequency or DC component. The modulating signal can be obtained effortlessly by employing a straightforward low-pass filter.

AM demodulation can be categorized into two main types: **synchronous** and **peak detector**.

Peak detection demodulation does not require synchronization with the carrier signal. Instead, it involves taking the absolute value of the modulated signal and then filtering out the high-frequency carrier components.

On the other hand, synchronous AM demodulation involves recovering the carrier signal from the modulated signal and multiplying it by a reference signal at the same frequency of the carrier. This allows for the recovery of the initial modulating signal, as the square of a sine wave can be broken down into a continuous component and a single sinusoidal component. Synchronous demodulation offers improved accuracy by eliminating distortion and noise. Furthermore, this type of demodulation allow to get the phase and therefore positive and negative field. However, it necessitates precise synchronization, typically achieved through the use of a specialized circuit called a phase-locked loop in order to match as much as possible the phase between the two multiplied circuits.

In simpler terms, synchronous demodulation requires synchronization which is complicated to achieve analogously because of the phase shift, while peak detection demodulation is simpler but may have limitations such as potential distortion and noise.

The next figure illustrate some design examples of synchronous and peak detection AM demodulation systems:

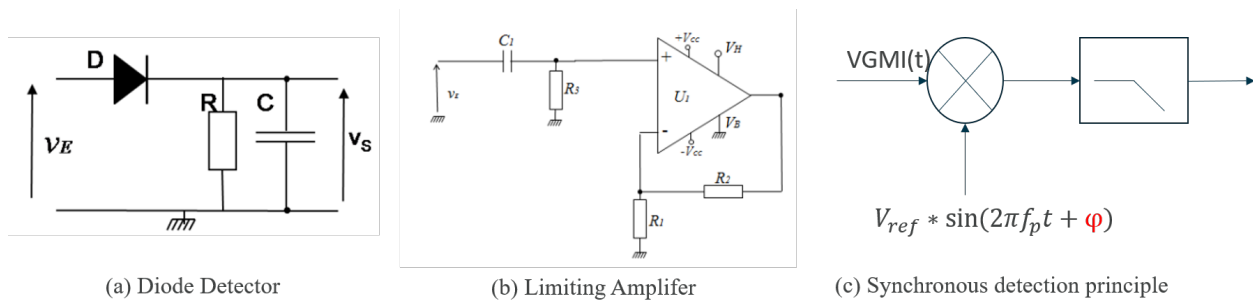


Figure 16: Exhaustive list of demodulation systems

Based on the provided information about different AM demodulation systems, let me explain the pros and cons of some demodulation systems:

1. Diode Detector: While the diode detector is simple to implement, it has some limitations. It is affected by temperature dependency, which can introduce variations in the demodulated output. Additionally, the diode voltage possesses a voltage threshold which limits its ability to accurately measure small fields. These factors make it less suitable for our detector if we need precise measurements and stability.
2. Limiting Amplifier: The limiting amplifier presents several advantages that establish it as a strong contender for our detector. Its operational principle involves removing the negative signal component and subsequently amplifying it. When combined with a low-pass filter, it becomes proficient at effectively detecting the modulated signal. One notable advantage is its capability to detect slight voltage or field variations efficiently, as it operates without a threshold, thus exhibiting high sensitivity. Additionally, it performs both demodulation and amplification concurrently, thereby reducing the overall system's complexity. Its straightforward implementation further contributes to its appeal, making it an attractive choice for practical applications.
3. Synchronous Detection: Synchronous detection, while capable of AM demodulation, presents some challenges. It is more complex to implement in analog form compared to other techniques. The requirement for the reference phase to match the GMI phase, which varies with the external field, adds another level of complexity.

Considering the limitations of the diode detector and the complexities associated with synchronous detection, the **limiting amplifier** stands out as the most suitable choice for our detector.

3.3.4 Amplification system

Amplification blocks in the readout circuitry play a crucial role as they significantly affect both the overall sensitivity of the output and the noise characteristics of the sensor. To minimize the circuitry required in our sensor design, it is advantageous to integrate the amplification functionality into other blocks, such as the demodulation block (Limiting amplifier) or when handling offset correction. This strategic integration allows for a more efficient utilization of resources.

In the simulation section, we will explore an example of a precision instrumentation amplifier with resistor gain programmability. This amplifier not only provides high accuracy but also offers the capability to adjust the offset, thereby allowing for precise offset correction.

3.3.5 Chosen sensor topology

To summarize what has been discussed in the preceding section, here is the topology of the sensor that we will simulate and construct throughout the course of this internship.

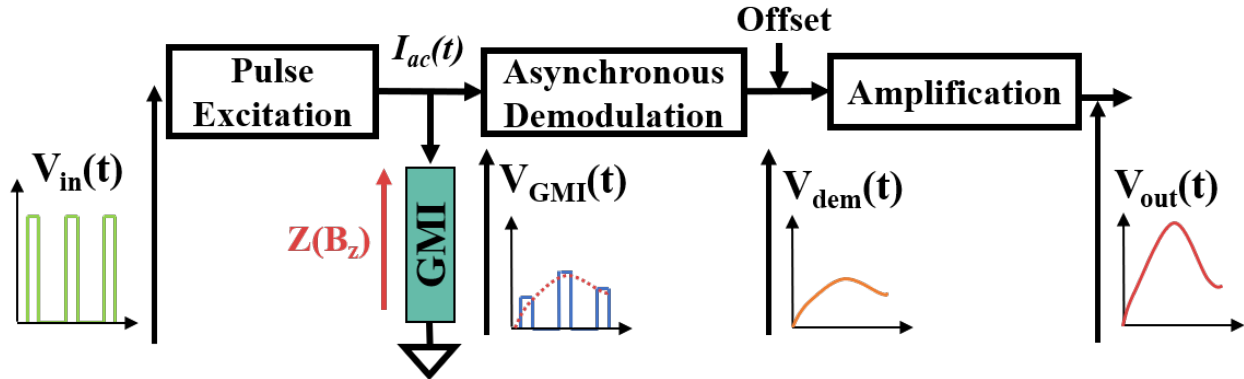


Figure 17: Chosen GMI sensor block diagram

1. The first block encompasses **the excitation system** based on an **RC oscillator** which provides a pulse current ($I_{ac}(t)$) to the sample ensuring supposedly high sensitivity for a low RMS current.
2. Next, we have **the sample** itself made of a vitrovac.
3. The **demodulation block** relies on an asynchronous demodulation obtained with a limiting amplifier followed by a **2nd order low-pass filter** to remove the harmonics.
4. **Amplification and offset correction.**

4 Simulation

In this crucial section, we will thoroughly explain the operation of each component of the sensor through LTspice simulation. We will utilize a specific model based on the components we have selected. Moreover, we will showcase two types of sensors: one based on GMI and another based on a dual GMI configuration. By providing detailed insights into their functionality, we aim to enhance understanding and demonstrate the versatility of these sensor designs.

4.1 Single GMI sensor

The initial sensor design will rely on a single GMI sample as its foundation. The excitation system will be comprised of a tunable RC oscillator, which will be followed by a pulse width modulator that utilizes a high-frequency comparator and buffer components to isolate the block effectively. For demodulation, a limiting amplifier will be employed to eliminate negative voltage and amplify the signal obtained from the sample. Additionally, a second-order low-pass filter will be integrated to attenuate unwanted harmonics. To address offset issues, an offset corrector based on a precision instrumentation amplifier with resistor gain programmability will be incorporated into the sensor's circuitry. These combined components will ensure accurate signal processing and offset correction for optimal performance. You can have a first overview of the sensor by looking first [Figure 18](#) below:

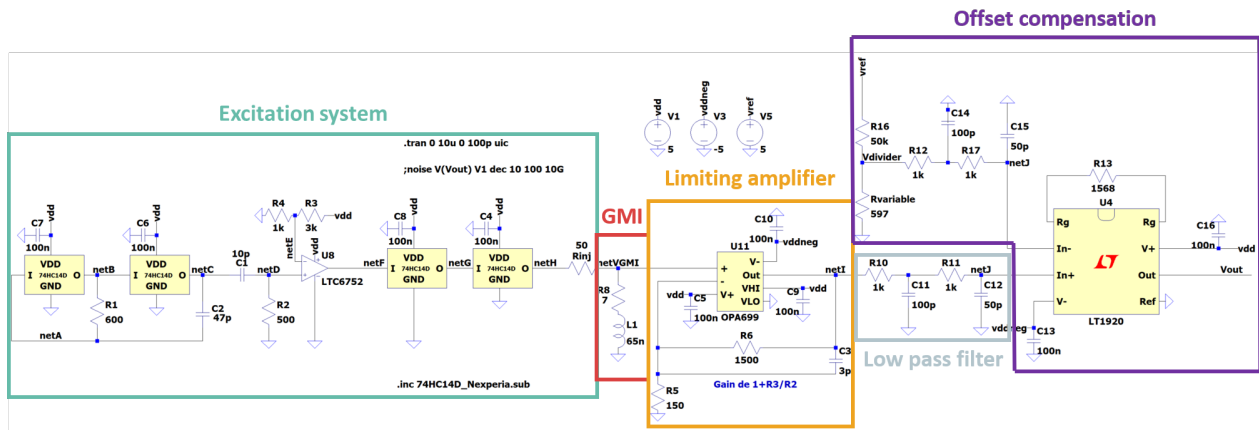


Figure 18: Overall sensor with one GMI

4.1.1 Excitation system

Figure 19 illustrates the complete excitation block, which is depicted below. The yellow boxes represent inverters that are implemented using the analogic model of the Hex inverting Schmitt trigger 74HC14 from Nexperia. For reference, the spice model of this inverter can be found in the annex (see Figure 64).

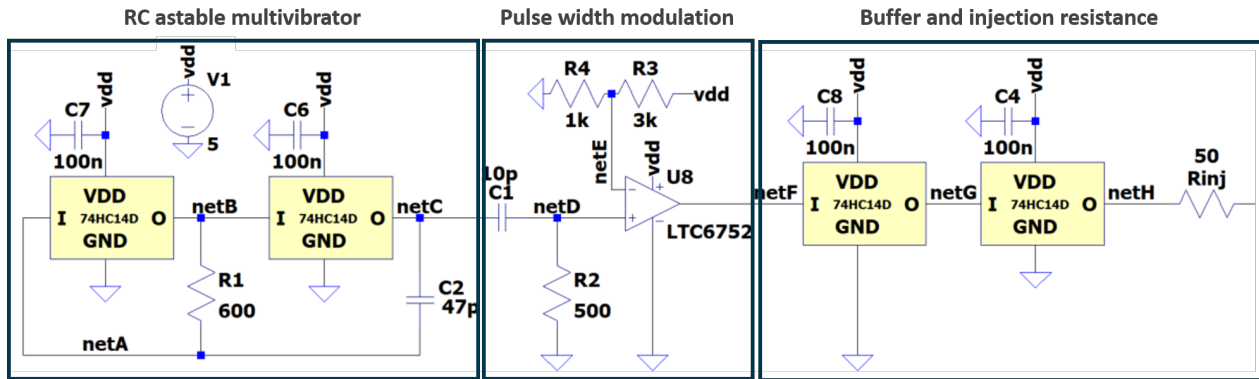


Figure 19: Entire Excitation system

Next, we will analyze each of these blocks individually by presenting simulation curves for the key nets within the sensor. All the Net of the next paragraphs are base on Figure 19

4.1.1.1 RC astable multivibrator

The initial component of the system consists of an RC astable oscillator (see left of Figure 19), which utilizes two inverters along with a resistor and a capacitor to determine the frequency of this basic square oscillator. The inverters are powered by a 5V DC voltage source, and decoupling capacitors are incorporated at the +5V input to minimize any alternating voltages originating from the power source.

Here are the curve result for the 3 important net that compose the astable oscillator:

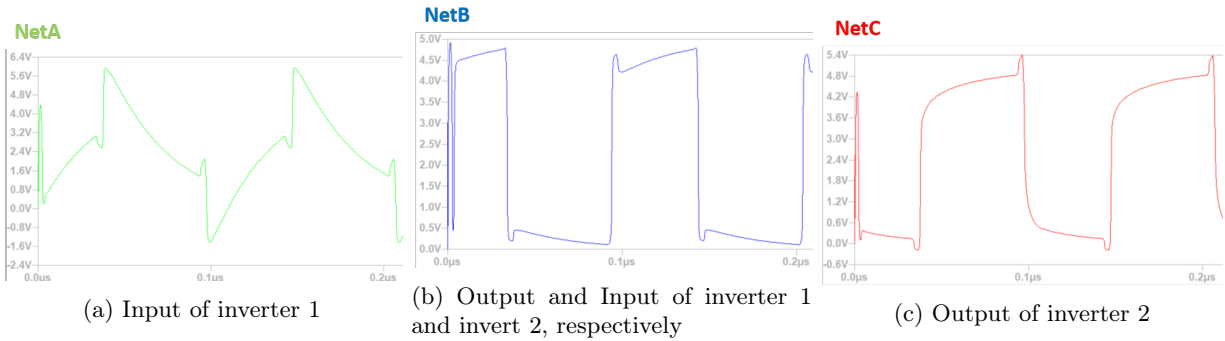


Figure 20: Spice curve of RC astable multivibrator

RC astable oscillator is a type of oscillator circuit that generates a square wave output without the need for an external trigger. In this circuit, the resistor (R1) and capacitor (C2) values determine the timing characteristics and frequency of the square wave output (here a value of approximately 9MHz).

The circuit operates as follows:

1. Initially, both inverters in the astable oscillator are in stable states. Let's call them "1" and "2."
2. Inverter 1's output is connected to the input of inverter 2, and vice versa.
3. The capacitor C charges through the resistor R, causing the voltage across the capacitor to increase.
4. Once the voltage across the capacitor reaches a certain threshold, it triggers inverter 1 to change its state, resulting in a change in its output.
5. This change in inverter 1's output is then fed back to the input of inverter 2, causing it to change its state as well.
6. As a result, the voltage across the capacitor starts to decrease as it discharges through the resistor.
7. When the voltage across the capacitor reaches another threshold, it triggers inverter 2 to change its state, thus completing one cycle of the square wave.
8. The cycle repeats as the process starts again, with inverter 1 being triggered and then triggering inverter 2.

The values of the resistor (R) and capacitor (C) determine the time it takes for the capacitor to charge and discharge, thus setting the frequency of the square wave output. By adjusting the values of R and C, it is possible to control the frequency of the oscillations generated by the RC astable oscillator. Here we designed R1 and C2 to have 9MHz frequency.

4.1.1.2 Pulse width modulation

After designing the RC astable oscillator, I developed a pulse width modulator. In fact, adjusting the pulse width is an effective method for fine-tuning both the RMS current passing through the GMI and the duration of sample excitation. This modulator consists of a C-R filter that takes the square wave output from the RC astable oscillator as its input. The output of the C-R filter is then connected to a high-frequency comparator. This comparator compares the voltage from the C-R filter with another reference DC voltage. By comparing these two voltages, the comparator generates a pulse output with a width that can be adjusted by altering the value of the reference voltage. By decreasing the DC voltage, the pulse width in the output signal will increase, leading to a higher overall power. Conversely, increasing the DC voltage will result in a narrower pulse width, resulting in reduced power.

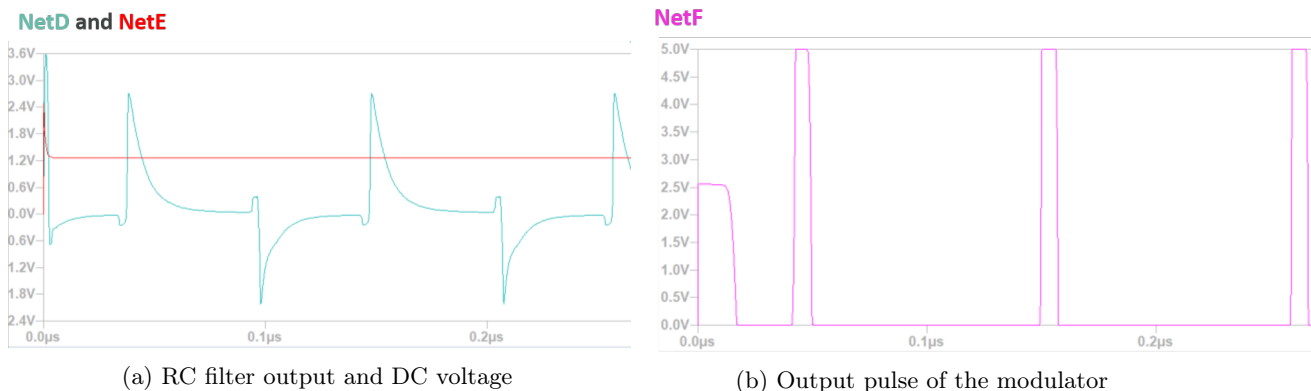


Figure 21: Spice curve of the pulse width modulator

Essentially, the C-R filter in the pulse width modulator acts as an intermediary stage that transforms the square wave output into a capacitor discharge curve. This capacitor discharge curve becomes the basis for obtaining pulse width modulation. Furthermore the C-R filter helps shift the DC level of the square wave to a suitable range for the subsequent stages of the pulse width modulator. This ensures compatibility with the high-frequency comparator, which typically requires inputs within a specific voltage range. In this setup, we have selected the LTC6752 high-frequency comparator. This specific comparator is capable of handling input signals of up to 280 MHz

4.1.1.3 Buffer and injection resistance

For this specific application, a buffer consisting of two inverters is employed to ensure a distinct separation and isolation between the excitation block and the remaining components of the readout circuitry, as well as the GMI sample.

The buffer operates by receiving the output signal from the excitation block and amplifying it while maintaining a high input impedance and low output impedance. This configuration helps to minimize any signal distortion or degradation during transmission to the subsequent stages of the circuitry.

Overall, the buffer serves as a protective interface, guaranteeing the integrity and isolation of the excitation block while safeguarding the proper functioning of the readout circuitry and the GMI sample.

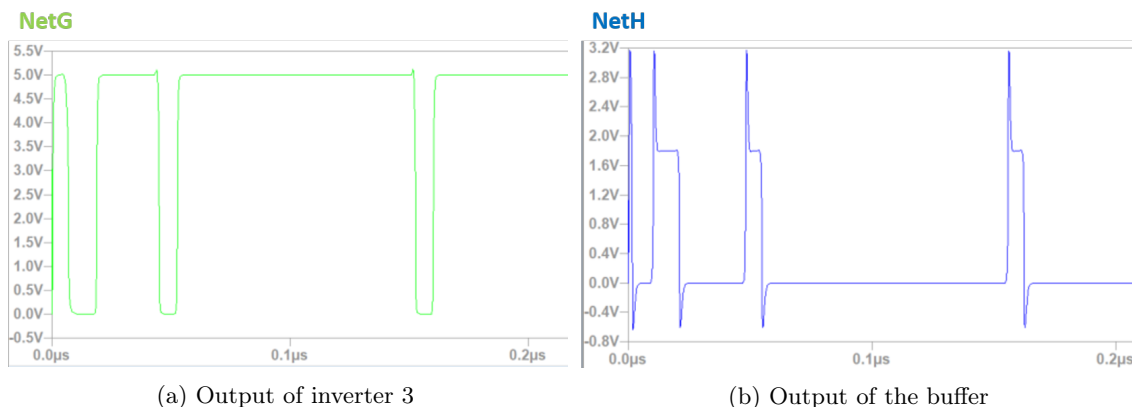


Figure 22: Spice curve of the output of the buffer

As anticipated, netG exhibits the exact inverse of netF. The output of the buffer is represented by netH. However, due to the connection of the net after the resistance R_{inj} to the GMI sample, the output of the excitation system is already influenced. This influence manifests as a reduction in the pulse amplitude and the appearance of peaks, primarily caused by the inductive characteristics of the GMI sample. The purpose of the injection resistance is to tune the value of the Iac pulse current generated in order to be in the condition explained in the previous paragraph 3.3.2.1. The curve resulting from the injection resistance will be presented in the next section.

4.1.2 Sensitive Element

In the LTspice simulation the sensitive element was modeled using a resistance and coil in series ranging respectively [3,7] Ω and [39,65] nH. The next Figure 23 highlight the voltage across the GMI and an exhaustive chart of the different value for the resistance and inductance of the GMI.

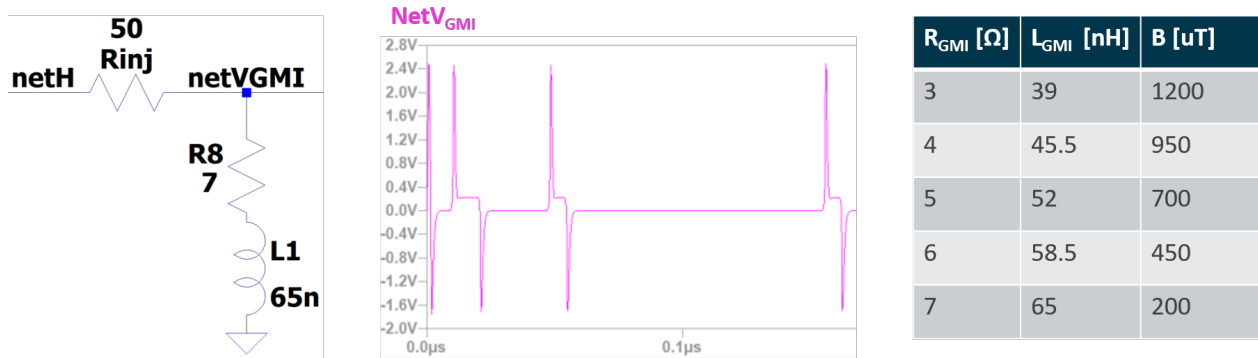


Figure 23: GMI spice model, GMI voltage, GMI impedance for different magnetic field

To ensure a constant current amplitude in the GMI, we must use an injection resistance that is at least three times the impedance of the GMI. This is necessary for injecting current effectively as discussed previously in the report.

To meet our current requirements, we have a budget of 10mA for AC and biasing combined. Our objective is to achieve a target of 5 mA rms for the AC current by employing pulse injection, which should supposedly allows us to attain high peaks while maintaining a low rms current. Through this approach, we aim to evaluate the potential enhancement in sensitivity. Thus, we are adjusting and optimizing the setup to ensure a consumption of 5 mA rms for the AC current.

4.1.3 Demodulation

In this subsection, we will explore the demodulation block, which comprises a cascaded setup of a limiting amplifier and a second-order low-pass filter. Figure 24 provides a visual representation of this block. For the limiting amplifier, we utilized the OPA699 model from linear technologies, which is detailed in the appendix of this report (Figure 65).

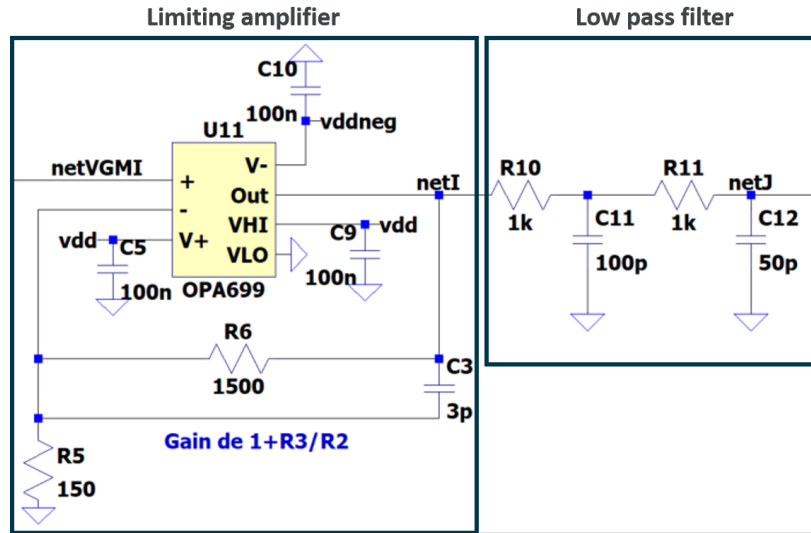


Figure 24: Spice Demodulation Block

4.1.3.1 Limiting amplification for demodulation

The limiting amplifier serves a dual purpose by functioning as both an amplifier and a signal rectifier.

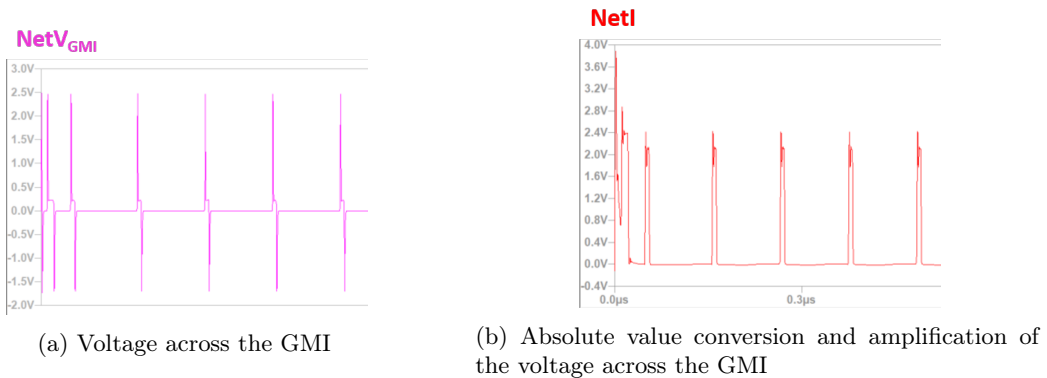


Figure 25: Limiting amplifier rectifying curve

Its gain, denoted as G_{opa699} , can be calculated as $1 + \frac{R6}{R5} = 6$ in this particular case. Additionally, we incorporate a small capacitance in the feedback loop of the limiting amplifier. This capacitor serves the purpose of reducing the spike of the pulse signal, ensuring a more stable output.

After eliminating the negative voltage component, our next step is to eliminate the unwanted harmonics and achieve a smooth, varying DC voltage output. To accomplish this, we introduce a low-pass filter with a cutoff frequency near the desired sensor bandwidth. In this case, the cutoff frequency will be approximately 1 MHz. This filtering process helps to maintain the desired signal while suppressing higher-frequency components, ensuring an accurate output for the intended application.

4.1.3.2 Low pass filter

The intention behind integrating this second-order low-pass filter is to eliminate undesired harmonics from the signal and capture only the components that depict modulation through the magnetic field. The cutoff frequency of the filter is approximately 920 KHz at -3 dB. The selection of the cutoff frequency is crucial as it determines the passband of the final sensor. By appropriately setting the cutoff frequency, we can ensure that the desired frequency components are preserved while attenuating higher frequencies, ultimately achieving the desired signal fidelity and accuracy in the sensor output. Although the cutoff is set at 1 MHz, we still noticed residual oscillation occurring at the pulse frequency, which originates as a remnant of the carrier signal.

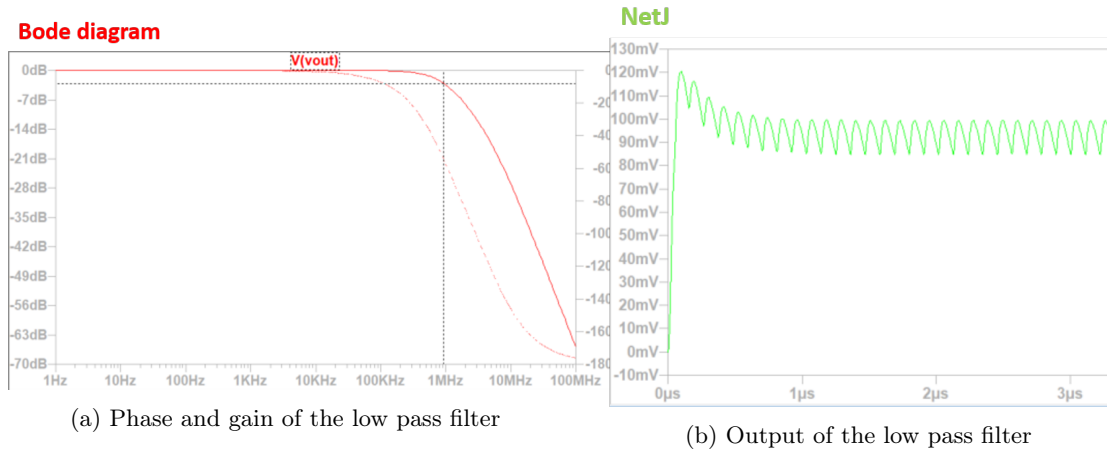


Figure 26: Low pass filter spice curve

Given that we are working with a single GMI that operates within its linear region on the impedance curve, it is necessary to subtract the voltage value corresponding to the null external field from the netJ. This step allows us to accurately measure the desired response of the GMI sensor by effectively eliminating any potential offset caused by the external bias field.

4.1.4 Offset correction

The final stage of the readout circuit serves the purpose of acquiring the ultimate output from the sensor. Specifically, the offset is utilized to establish a zero voltage output at zero external magnetic field. The offset voltage can be adjusted using $R_{variable}$ as shown in Figure 27. Subsequently, the amplified final output, which is the difference between NetJ (net coming from the low pass filter) and NetK (tunable constant voltage), is subjected to further amplification. This amplification is accomplished using the following gain formula: $G_{LT1920} = 1 + \frac{49.9k}{R13}$. By applying this gain, we can enhance the magnitude of the final output signal, facilitating improved signal processing and analysis.

Here is the last block of the sensor based on the LT1920 differential amplifier:

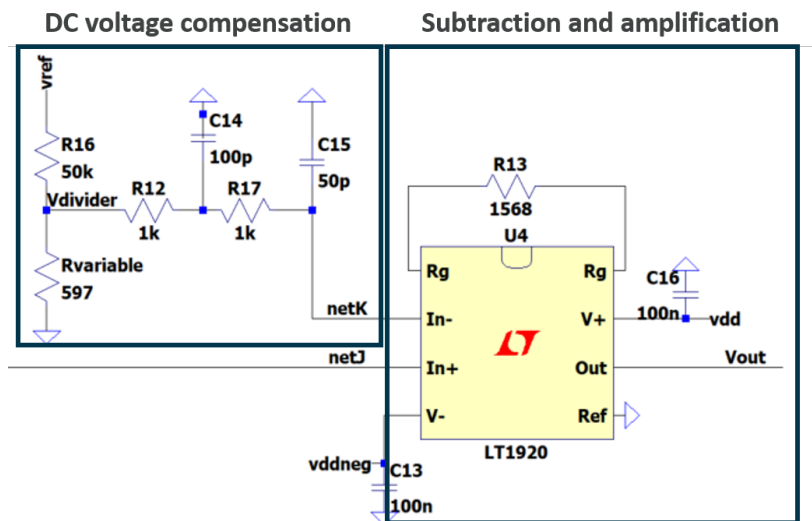
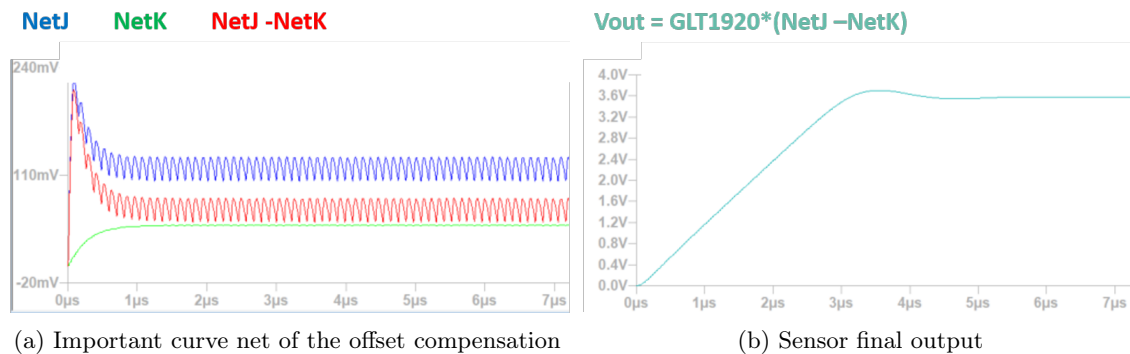


Figure 27: Offset and amplification block

In the netK section with the voltage divider, we incorporate the same low-pass filter to ensure better alignment when subtracting netJ and netK. By applying this filter, we aim to achieve improved coherence and accuracy between the two nets. The difference between the two nets is subsequently amplified to obtain the final sensor output within the desired range, determined by the chosen gains (G_{opa699} and G_{LT1920}).



(a) Important curve net of the offset compensation

(b) Sensor final output

Figure 28: Final block output

In the output displayed in Figure 28b, a form of overshoot is noticeable prior to the stabilization of the DC voltage. This phenomenon is a result of the transient behavior of the calculation and is exclusive to the simulation, without any anticipated impact on the experimental response time. This underscores the model’s limitations in terms of simulation accuracy.

4.1.5 Simulation of calibration

The calibration process for the sensor involves the following steps:

1. Bias: We initiate the calibration by simulating the application of a magnetic field, denoted as H_{bias} , to the GMI sample. This field is carefully chosen to ensure that the GMI operates within its linear region, optimizing its performance (basically in simulation we put $R_{GMI} = 5 \Omega$ and $L_{GMI} = 52 \text{ nH}$).

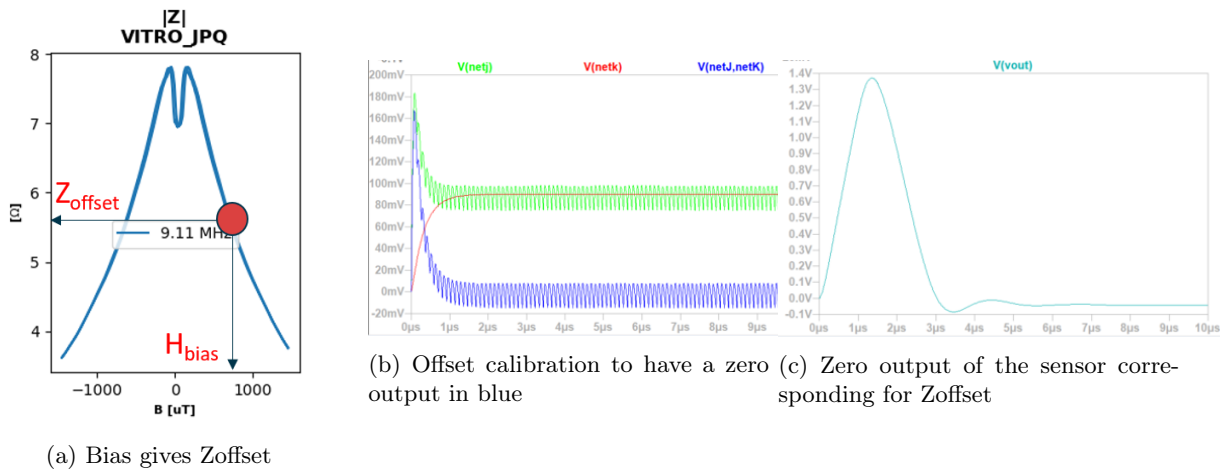


Figure 29: Some calibration steps

2. Power Consumption Adjustment: Next, we determine the desired power consumption for the sensor by fixing the values of R_{inj} and the pulse width of the oscillator (R4). This step allows us to achieve the desired balance between power consumption and sensor performance.
3. G_{opa699} selection: We carefully choose the gain of the limiting amplifier, denoted as G_{opa699} (R6), to achieve the desired amplification level for the sensor output. This step is crucial for enhancing the signal fidelity and ensuring optimal performance.
4. Offset Setting: To establish the appropriate offset, we set the value of NetK (Rvariable) to match the value of NetJ when the GMI's impedance is equal to Z_{offset} . This is achieved using specific values of resistance ($R = 5\Omega$) and inductance ($L = 52\text{nH}$) (half value of each range), ensuring accurate measurements in the presence of external magnetic fields.
5. G_{LT1920} fixing: We fix the value of G_{LT1920} to ensure a $+2\text{V}$ output when the GMI reaches its maximum impedance (for $R = 7\Omega$ and $L = 65\text{nH}$) and a -2V for when it reach the minimum impedance (for $R = 3\Omega$ and $L = 39\text{nH}$). This step allows us to align the sensor's output voltage range with the desired impedance range, facilitating accurate measurements and optimizing the sensor's overall performance.

By meticulously following this simulation calibration process, we can ensure the sensor operates reliably and provides accurate measurements within the specified operating conditions

4.1.6 Performance and noise

We can now plot on Itspice the expected output of our sensor based on the 5 values selected for our GMI from Figure 23 based on the precedent calibration with $G_{opa699} = 6$, $G_{LT1920} = 64$ and $V_{offset} = 89.13$ mV we obtain the following result:

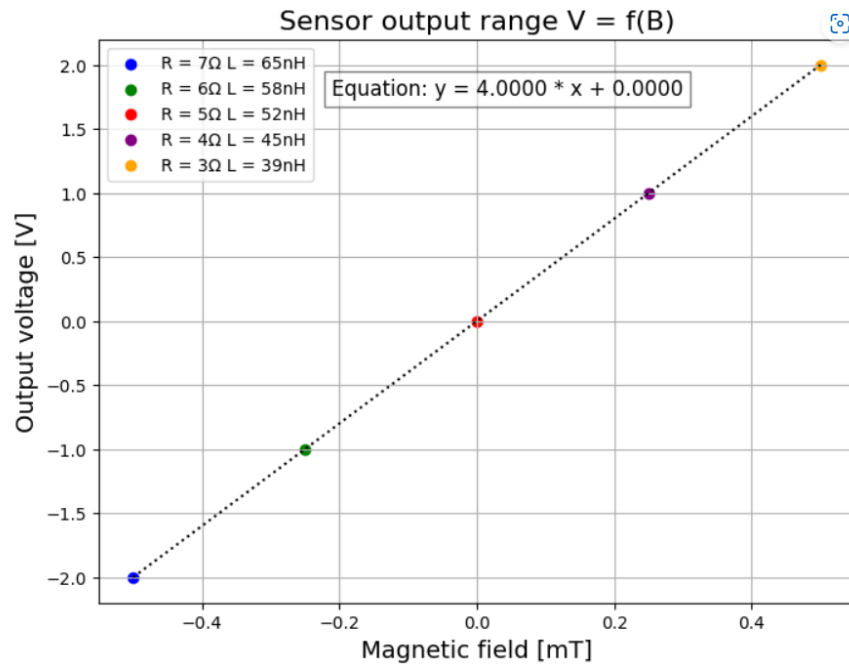


Figure 30: Sensor range output for different GMI value

At the highest voltage output, we reach this point when the sensor is experiencing the maximum module of impedance. This corresponds to the application of the maximum external negative field. Conversely, at the lowest output voltage, we observe the minimum value of the impedance module, indicating the detection of the maximum external positive field. In essence, the sensor's voltage output is inversely related to the impedance module, allowing us to distinguish between different external magnetic field polarities based on the observed output voltage levels. In this particular configuration, we achieve a voltage variation ranging from +2V to -2V, encompassing a field range of +0.5mT to -0.5mT. So the expected sensitivity is $S = \frac{4V}{1mT}$

To obtain a rough estimation of the system's overall noise, we utilize the noise study command in LTspice. We can analyze the noise characteristics by examining the voltage output (V_{out}) and applying a frequency sweep ranging from 1 Hz to 10 GHz, with a logarithmic step size of 10 point. This noise study allows us to assess the system's noise performance across a wide frequency range and gain insights into the noise contributions within the circuit. The obtained result, presented below, was obtained with a pulse current of 5 mA RMS.

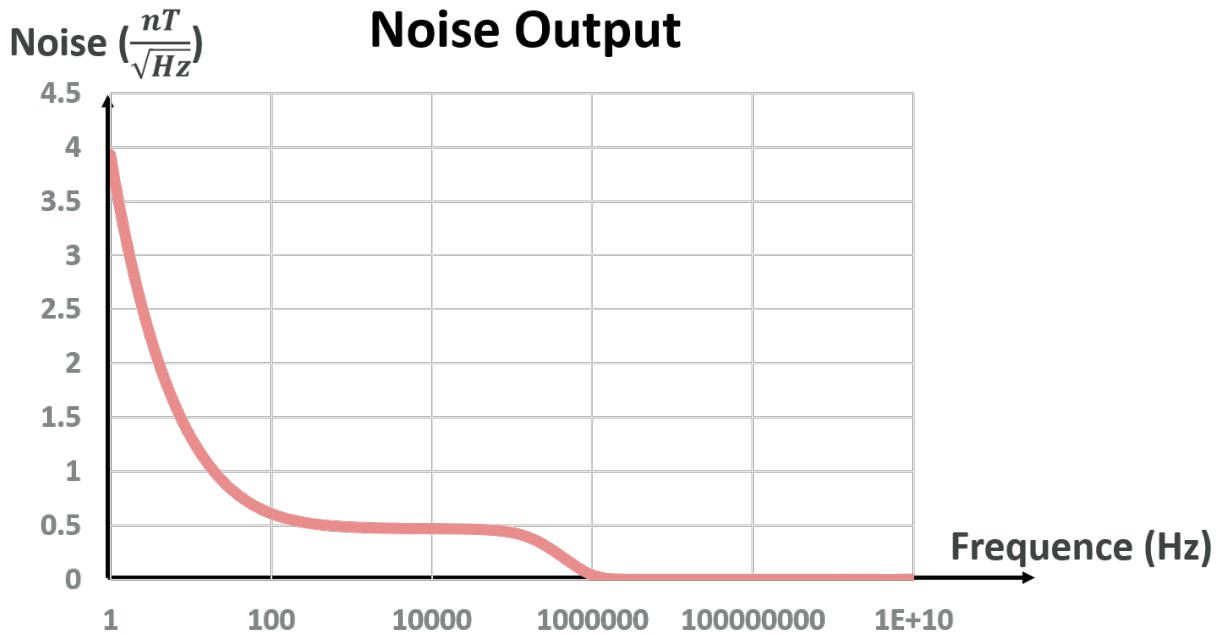


Figure 31: LTspice noise study

Figure 31 was obtained by multiplying the spectral density in $\frac{V}{\sqrt{Hz}}$ from Ltspace by the sensitivity of the sensor: $Noise(\frac{nT}{\sqrt{Hz}}) = Noise(\frac{V}{\sqrt{Hz}}) * \frac{Sensor\ field\ range}{Sensor\ voltage\ output\ range}$. The result obtained in $\frac{nT}{\sqrt{Hz}}$ is what we call the equivalent magnetic noise. We can make a rough estimation of the noise by using the value of the plateau at around 10kHz. This plateau serves as a reference point from which we can gauge the noise characteristics. We obtain for the red curve around $0.5 (\frac{nT}{\sqrt{Hz}})$.

Furthermore we can observe a distinct low-pass filter behavior at a frequency of approximately 1MHz. This behavior aligns well with the sensor's bandwidth, which was predetermined by the second-order low-pass filter cutoff frequency. The presence of this low-pass filtering effect suggests a coherent and consistent response from the sensor, allowing us to effectively filter out high-frequency noise and focus on the desired signal within the specified frequency range.

By multiplying the value of the noise plateau by the square root of the bandwidth frequency we obtain a noise of **500 nT** (RMS value).

4.2 Dual GMI sensor

In the concluding section of the simulation chapter, we will thoroughly examine the development of the dual GMI sensor. This exploration will involve analyzing two excitation system blocks and assessing the performance of the selected technology for the duration of this internship.

To recapitulate what has been previously discussed, the primary benefit of utilizing two GMI sensors is the ability to achieve a differential measurement. This approach directly eliminates the offset without requiring additional compensatory circuitry (Figure 7). You can have a first overview of the sensor by looking Figure 32 for a better understanding of what have been said. This figure highlight the global block diagram of the chosen spice sensor model with a dual GMI that we will be also building on pcb. The proposed approach involves the utilization of a dual RC astable oscillator as the foundation, followed by two demodulation chains

utilizing a limiting amplifier for each of the distinct sensitive elements. The desired output is obtained by subtracting the two DC voltages obtained from the two GMI samples.

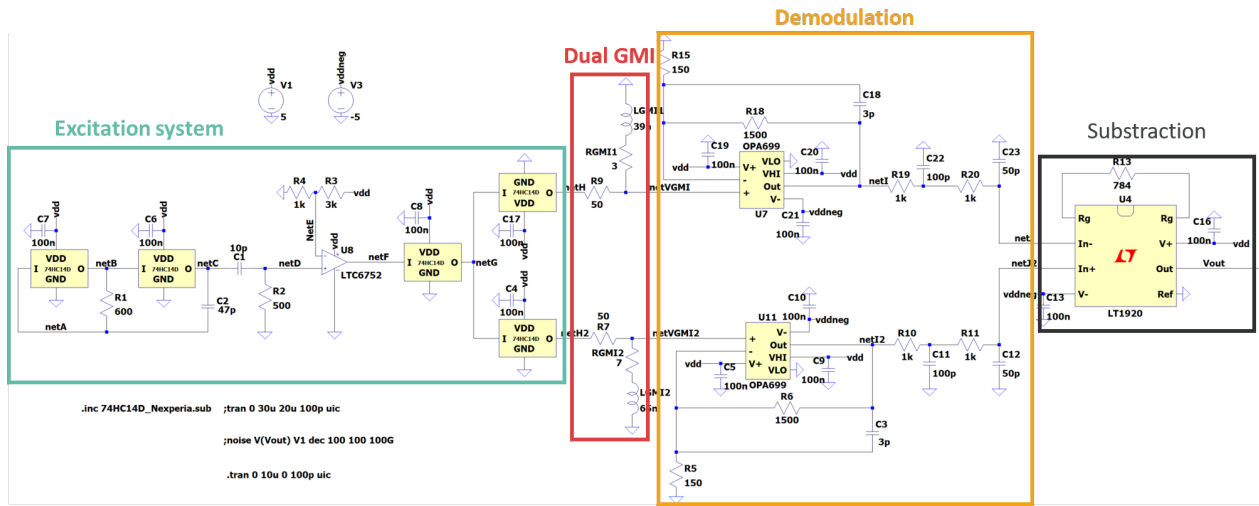


Figure 32: Overall sensor with two GMI

Since the circuitry is quite similar between the single and dual GMI, only the result of the excitation system will be presented below.

4.2.1 Dual RC Astable oscillator

As the previous paragraph it's possible by adding an inverter gate to build a suitable RC astable multivibrator that can drive two sensitive element.

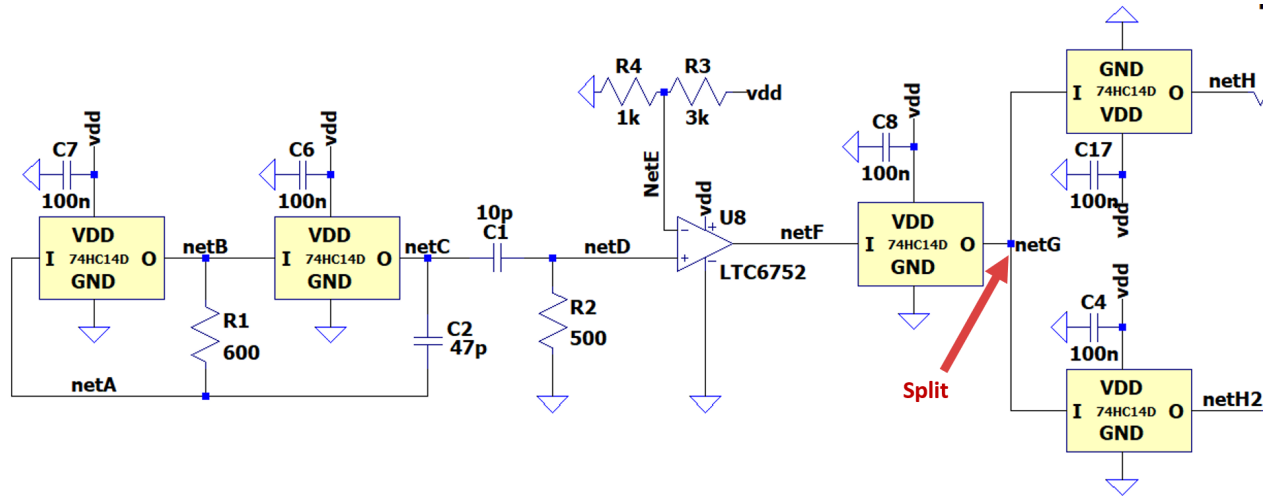


Figure 33: Dual astable oscillator

To achieve this, we simply divide the conventional RC astable oscillator into two branches within the buffer section. This division guarantees that the pulse current flowing through the GMI samples maintains a constant amplitude value. Having two GMI with opposite biasing ensure a linear regime for the sensor. Here

in Figure 34 are the voltage output across the two sensitive element with different value of impedance since they have an opposite bias:

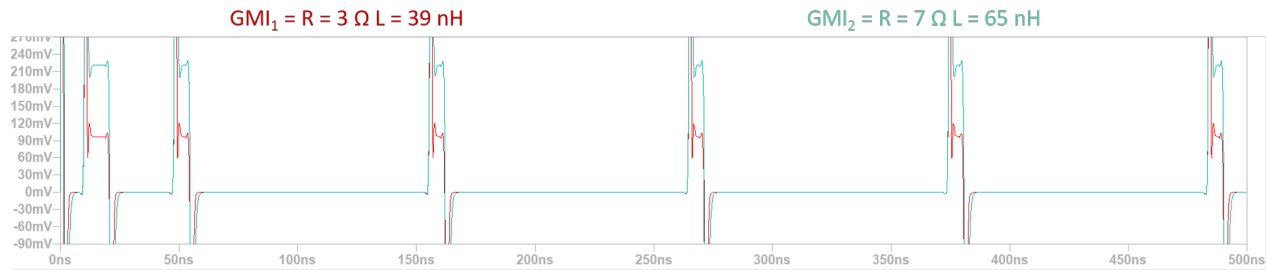


Figure 34: Voltage at the GMI samples

An **integrated dual GMI oscillator** as also been simulated and is present in the annex of this report.

4.2.2 Performance and estimated noise

The simulated calibration process fine-tunes the gain to achieve the desired value for an appropriate output voltage range. No offset correction is needed. An output range of +2V to -2V is selected, anticipating the sensor’s output to fall within this range. Here are the results when combining different impedance of the two GMI:

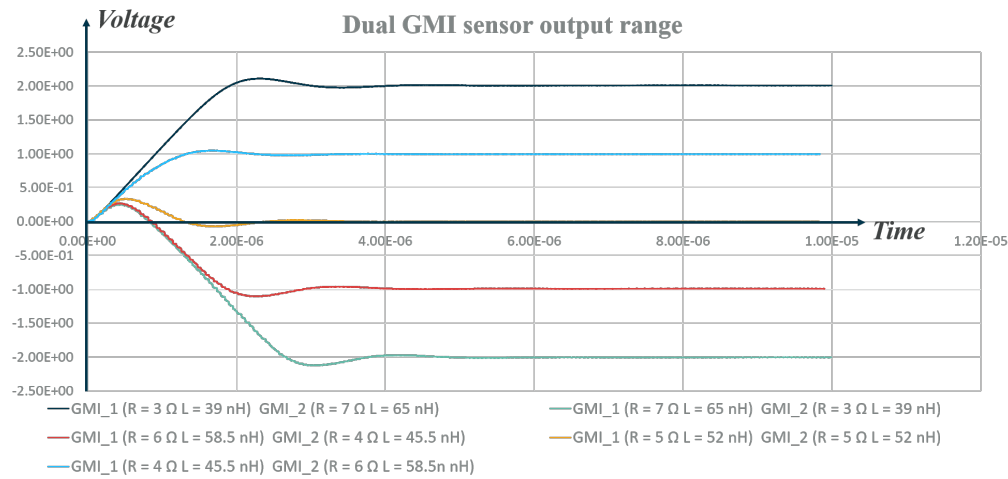


Figure 35: Dual GMI Sensor range output for different GMI combination

In a similar manner to the approach taken in the previous section for one GMI, we simulate the expected sensor noise in this particular configuration. The configuration involves a 5 mA RMS current for each GMI, achieved by tuning the R_{inj} (set to 150Ω in this case) to match the same 5 mA RMS current as that of one GMI.

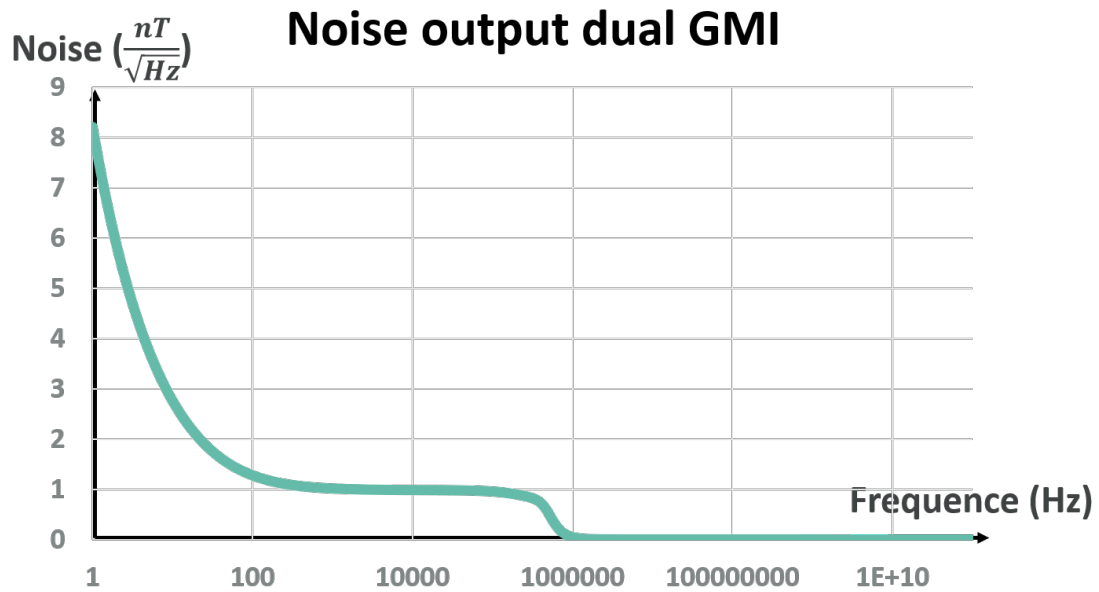


Figure 36: Noise for a dual GMI configuration

We obtain the curve in the same manner than [Figure 31](#) since the output voltage of our sensor and the magnetic field range is set to be the same than for 1 GMI. Due to the inclusion of a demodulation block with a significant gain, the expected noise outcome of combining two GMI will be higher compared to using only one, as the additional block will significantly contribute to the overall noise.

5 PCB design

In this crucial section, we will outline the process of designing the PCB using Altium software.

The PCB design was divided into two main parts:

1. The first PCB, referred to as the GMI Holder, was specifically created to accommodate and bias the GMI sensitive elements. See [Figure 38](#).
2. The second PCB connected and positioned beneath the GMI Holder PCB, was dedicated to housing all the electronics readout and excitation circuitry. See [Figure 39](#).

Through this two-part design, we aimed to ensure efficient organization and connectivity between the GMI sensitive elements and the associated readout circuitry. Additionally, we ensured that the PCB size is conveniently compact to facilitate its integration into the characterization setup.

5.1 GMI holder

Prior to starting the PCB design process, an initial investigation using COMSOL Multi-physics was carried out to design a flat coil capable of biasing the ferromagnetic sample up to 3mT in the Bx direction. The dimensions of the coil were determined, with a 20 mm length selected for our GMI. Opting for a flat coil enabled us to employ the standard PCB fabrication process, including deposition and via construction, for its efficient production.

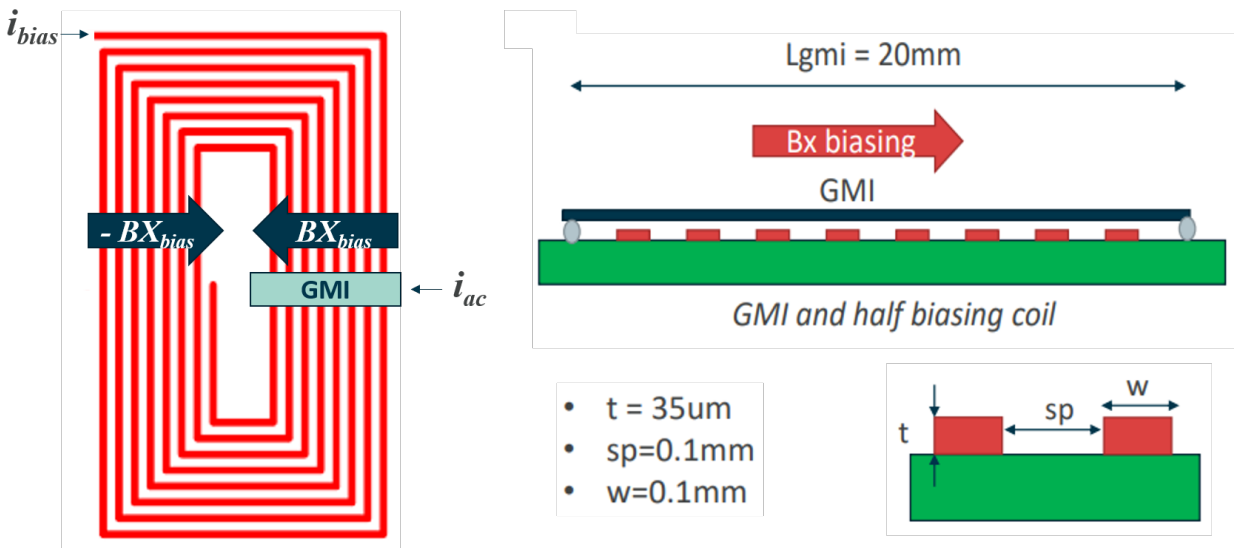


Figure 37: Biasing coil design

Based on a GMI length (L_{gmi}) of 20mm and utilizing the standard PCB process, it is possible to incorporate up to 100 loops within the design, resulting in a magnetic field sensitivity of 3.135 mT/A. In practical applications, for a biasing level of 1.5mT as determined through direct measurement, a current of 480mA would be required. Conversely, for a biasing level of 250uT obtained through magnetic derivation, a lower current of 80mA would be sufficient.

In addition to its primary function, the flat coil is capable of generating a higher magnetic field in the Z-axis direction, potentially leading to the occurrence of Foucault currents along the surface of the PCB. To mitigate their impact, a strategic approach will be implemented. A ground layer with linear inter-spacing

will be introduced on the top layer of the PCB, effectively dispersing these currents and minimizing their effects. By incorporating this protective measure, the adverse consequences of the generated magnetic field can be significantly reduced.

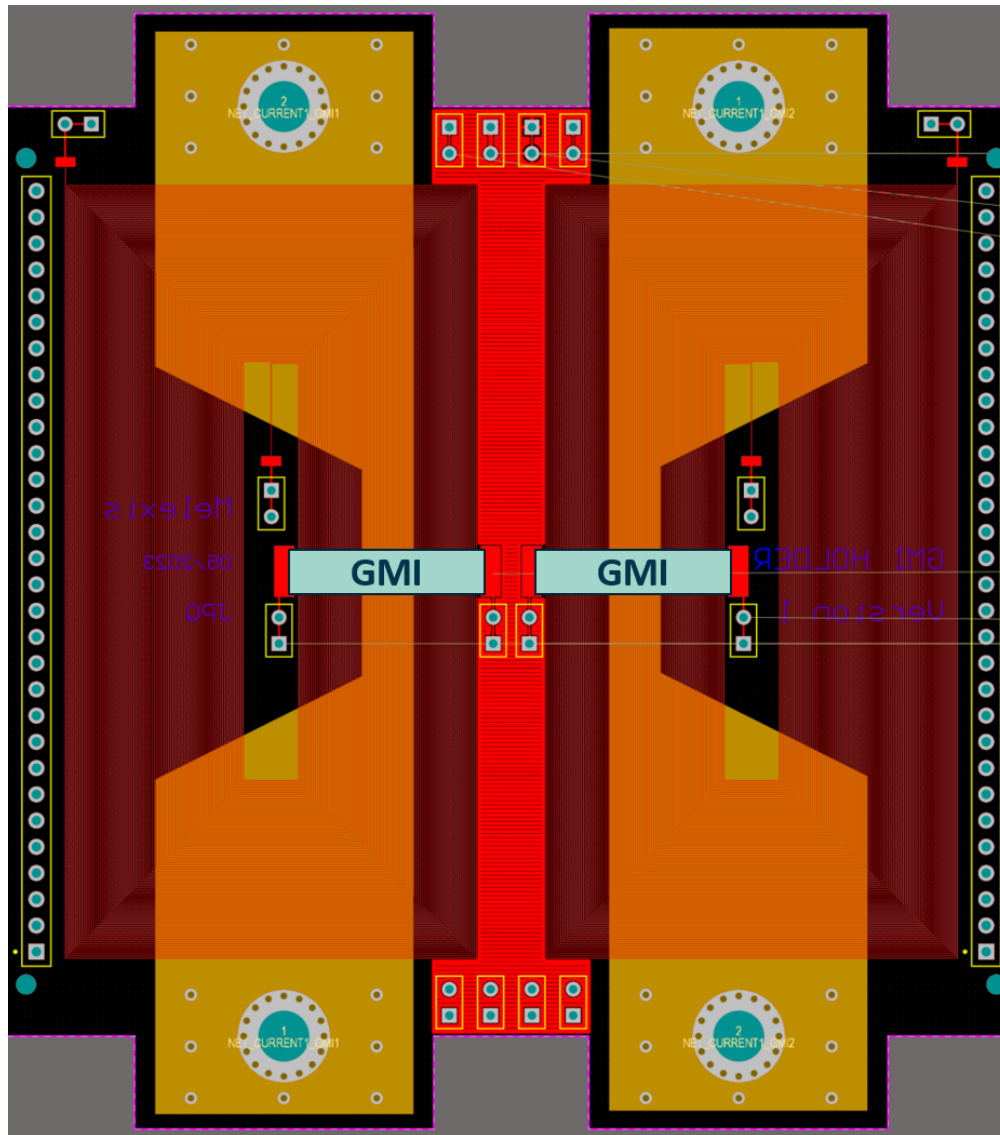


Figure 38: Altium GMI holder PCB

As depicted in [Figure 38](#), the PCB design incorporates two distinct GMI sections, each equipped with its respective bias flat coil (depicted in dark red). By accurately controlling the magnitude and orientation of the bias current, we can determine both the strength and direction of the magnetic bias field. In the central region (depicted in light red), a ground layer is implemented to effectively counteract the occurrence of Foucault currents. Additionally, the presence of three overlaid layers (depicted in orange-brown) enables the conduction of an external current. This current serves the purpose of real-time performance testing for our sensor, effectively demonstrating the operational functionality of our current sensor prototype.

5.2 Electronics

The final iteration of the PCB design encompassed the integration of all the sensor electronics. This design incorporated switches and variable resistors, providing the flexibility to utilize either one or two GMI elements in our sensor, as well as allowing fine-tuning of crucial parameters such as system frequency and gain. This configuration enables enhanced adaptability and optimization of the sensor’s performance according to specific requirements.

The provided image depicts the 3D representation of the PCB electronics, showcasing all the components, including switches that allows for changing the connection points of the GMI to either ground or to each other. This enables the usage of either one GMI or two GMI configurations

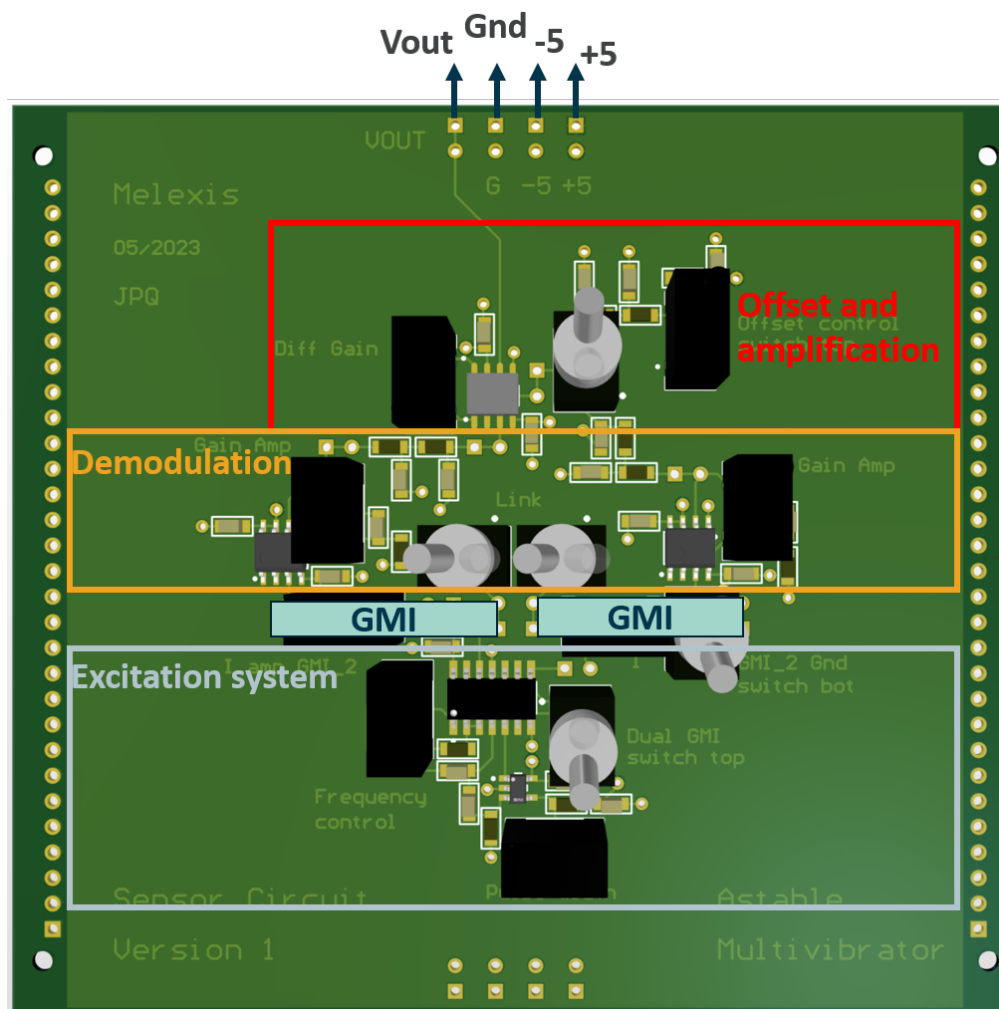


Figure 39: Altium electronics PCB

In the PCB layout, all components are positioned on the bottom layer. The remaining three layers are utilized for routing various connections, including the +5V, -5V, and ground connections. This segregation allows for efficient organization and optimal utilization of the PCB space. The two PCBs are interconnected using wires to facilitate the connection between the GMI sample and the electronics PCB effectively.

5.3 PCB result

During the internship, the actual PCB that was received from euro circuit and assembled is depicted in Figure 40:

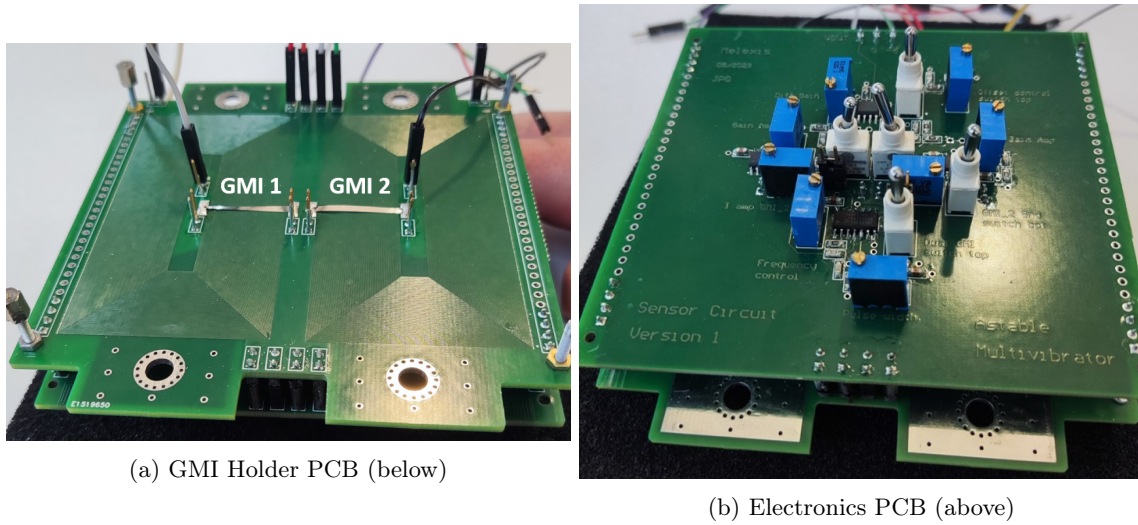


Figure 40: Final sensor PCB

On the right we can observe the two GMI with biasing coil right below. On the left is the circuit of the board. The two pcb are then connected one above each other. The switch can then be configured in order to use the sensor with 1 GMI or 2 GMI.

6 Characterization

This concluding section will focus on characterizing our demonstrator, encompassing various aspects such as the biasing coil, the characteristic impedance curve, and real-time current measurement.

6.1 3D Support and characterization of the biasing coil

A clear 3D printed support was designed to facilitate the measurement process by providing structural stability to the PCB and seamlessly integrating into the characterization setup (see Figure 61)

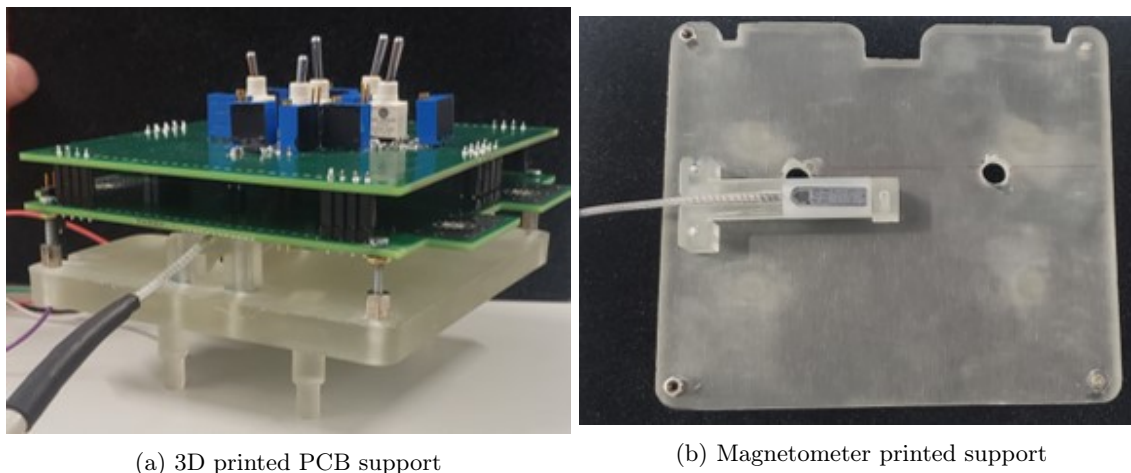
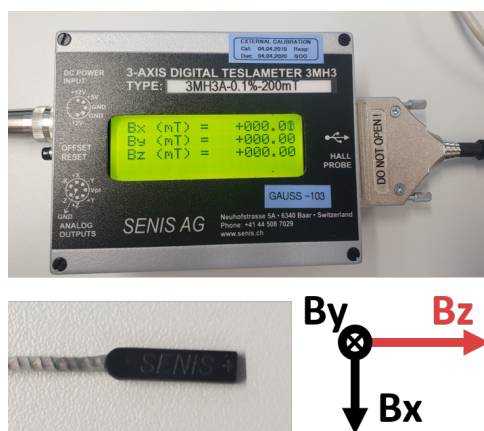
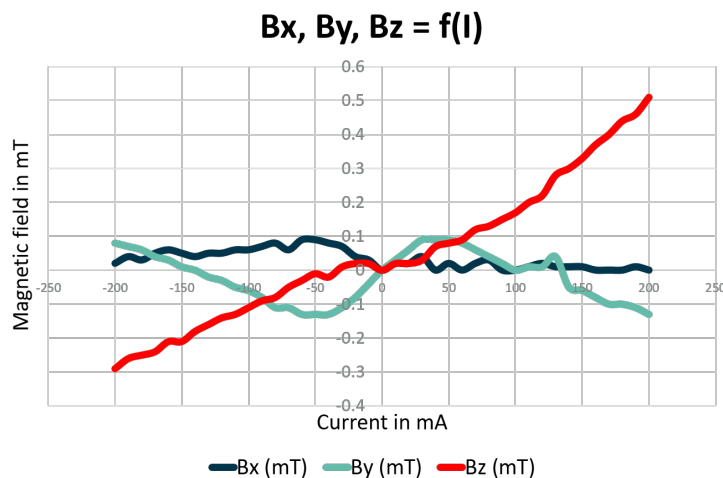


Figure 41: 3D printed pieces

A support was specifically designed for the magnetometer to ensure its proximity to the GMI sample. This close proximity allows for capturing the value of the B_z field provided by the coil, which will be crucial for determining the biasing range of the printed coil. The SENIS gauss 103 magnetometer is employed to provide a rapid assessment of the biasing strength of our coil.



(a) Senis Gauss 103 Magnetometer



(b) B_x, B_y, B_z measurement

Figure 42: Biasing coil measurement across the GMI

As depicted in Figure 42b, the biasing coil demonstrates its capability to generate a magnetic field of 0.5 mT when a 200 mA current is applied, corresponding to approximately 2.5 mT/A, which aligns with the estimated simulation. However, it is important to note that at higher current levels, the temperature of the PCB significantly rises, leading to a potential risk of coil damage. Therefore, it is necessary to avoid continuous current biasing and instead limit its application to short duration during the measurement process.

6.2 Impedance characterization setup and first functioning result

The initial arrangement (refer to Figure 61) was designed to investigate the impedance characteristics by utilizing the strong magnetic field generated by the coil. This particular configuration was necessary because the printed coil on the PCB did not produce a magnetic field of sufficient strength to fully capture the curve. Consequently, this setup has the capability to generate a magnetic field ranging from -1.5 mT to +1.5 mT.

The Python script in Spyder was used to control various measuring instruments. The instruments included in the setup were as follows:

1. KEITHLEY 2231A-30-3 : To provide the +5 V and -5 V for the PCB
2. 2 KEITHLEY 2400 : One to furnish the current for the biasing coil and one to acquire the output signal
3. 3 RIGOL DP832 : To provide the current in the 3 coils of the Helmholtz
4. 3 Keithley 2000 : To measure the current in the 3 coils of the Helmholtz setup

For the first measurement of the impedance curve there was no need for a biasing since we want to obtain the overall impedance curve.

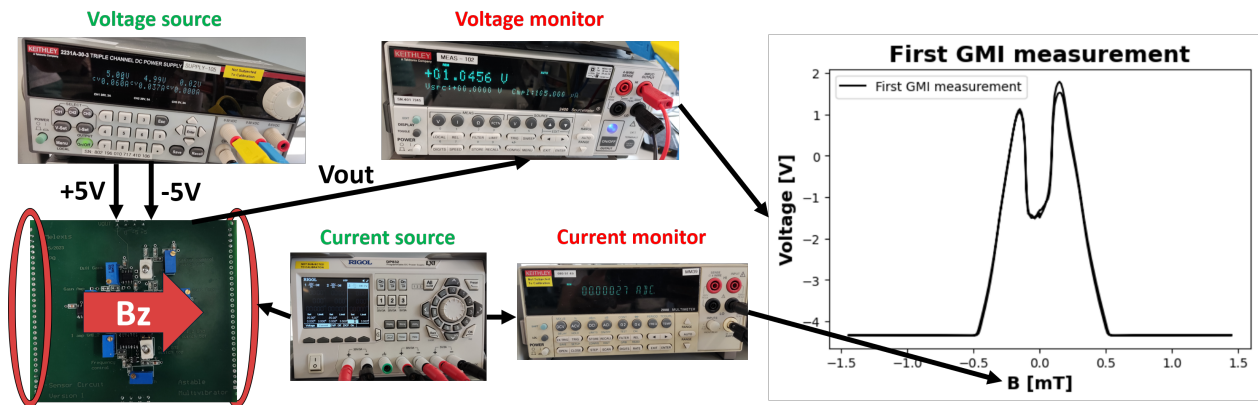


Figure 43: Helmholtz setup

6.3 First sensor result using the Figure 43 setup

The aim of this paragraph was just to validate the sensor behaviour using a magnetic biases from Helmholtz coil as the input of our system.

6.3.1 1 GMI configuration

Utilizing the configuration described in Figure 43, we initially derive the impedance curve that characterizes 1 GMI . Following the determination of the optimal bias for our sensor using the impedance curve (around 0.5 mT)

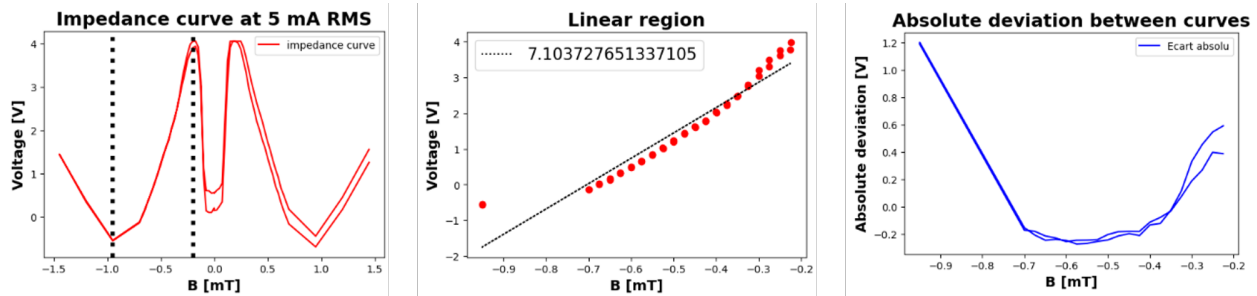


Figure 44: Impedance caractéristique, linear domain, and absolute deviation at 6 MHz, 5% duty cycle

The impedance curve shape which correspond to our expectation exhibits a linear region spanning approximately 750 uT, with a sensitivity of approximately 7.1 V/mT. The absolute deviation increase on the edges of the linear region.(The measurement was performed in a back-and-forth manner: -1.5, +1.5, -1.5mT).

6.3.2 2 GMI configuration

We begin the characterisation with the 2 GMI configuration by an analysis of the linear region voltage output depending on the magnetic field value produce by the two biasing coils (using the setup of Figure 43). You can find below the curve shape:

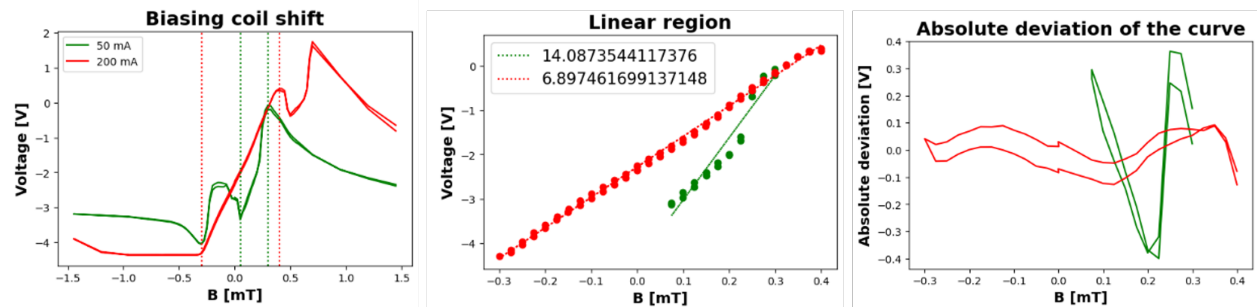


Figure 45: Impedance characteristic for different opposing current Green = 50 mA, Red = 200 mA - $G_{opa699} = 11, G_{LT1920} = 100$, 6 Mhz pulse and 15% duty cycle

After determining the magnetic linear range for both curves, we opted to bias the sensor at 200 mA (around 0.5 mT) in the next measurement due to its broader range of 700 uT and better linearity compared to the 250 uT range when biased at 50 mA. Reducing the sensor’s gain may allow detecting a higher range of magnetic fields without saturating at the curve’s edge, although the offset in the dual GMI configuration cannot be controlled. The impedance curve’s shape aligns with our expectations (see Figure 7). However, using a higher bias could increase the linearity but would risk damaging the PCB. Additionally, the disparities in the 2 GMI samples used played a crucial role in shaping the observed impedance curve.

6.4 Impedance characteristics for different configuration

In this section, we will examine the impedance curve and sensitivity of the 1 GMI configuration and 2 GMI configuration by exploring various factors that influence it. These factors include the gain of the overall system (G_{opa699} , and G_{LT1920}), the frequency, the amplitude, and the duty cycle. In this paragraph we will still be using the Figure 43 setup

6.4.1 Duty cycle variation

Since we have allowed for flexibility in the PCB design to modify the excitation system, our initial focus will be on studying the existing excitation system present on the board, which is the pulse oscillator. The following adjustments in duty cycle and frequency will be carried out while maintaining fixed gain values of $G_{opa699} = 20$ and $G_{LT1920} = 115$. In this paragraph, we will conduct a duty cycle shift ranging from 5% to 20% at a pulse frequency of 6 MHz.

6.4.1.1 1 GMI configuration

During the measurement, the biasing coils will transition from -1.5 mT to 1.5 mT and then return to -1.5 mT. This is done to observe any potential output drift caused by temperature rise or component instability.

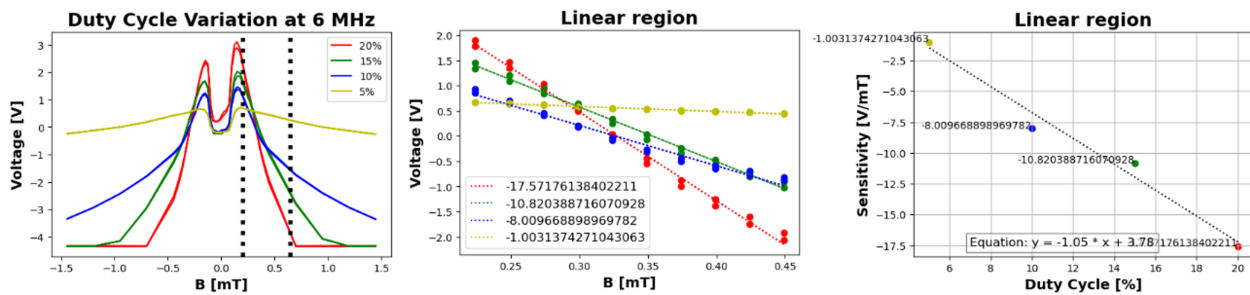


Figure 46: Red = 20% Green = 15% Blue = 10% Yellow = 5% duty cycle

The linear region was determined to be between 0.2 mT and 0.65 mT, aligning with the linear region of the most sensitive curve (the red one), which covers approximately **450 uT of working range** before saturating. According to the graph, higher duty cycles result in higher sensitivity but a reduced detectable magnetic range as the sensor's output saturates faster. The respective sensitivities are as follows: **17.5 V/mT**, **10.8 V/mT**, **8 V/mT**, **1 V/mT** for duty cycles of 20%, 15%, 10%, and 5%. Notably, the obtained sensitivities appear to increase linearly.

6.4.1.2 2 GMI configuration

We then performed in the same condition the duty cycle shift for the dual GMI configuration. Indeed, we choose the same delimitation of magnetic field range which was of 450 uT. The observe result were quite similar to the 1 GMI with a variation of 1.08 [V/mT/%] against 1.05 [V/mT/%] for the 1 GMI.

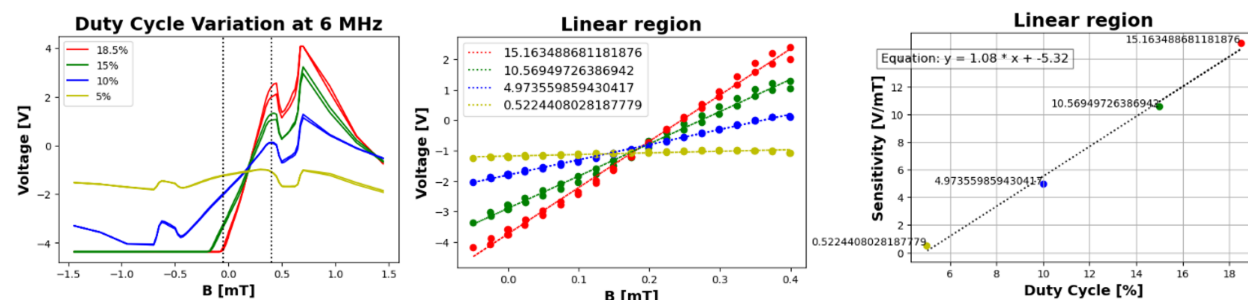


Figure 47: Red = 18.5% Green = 15% Blue = 10% Yellow = 5% duty cycle

6.4.2 Gain shift variation

In this paragraph we will perform a similar analysis as the duty cycle but with the gain. This time we will fix the value of the duty cycle at 15%, the frequency at 6MHz and modify the product $G_{opa699} * G_{LT1920}$ in both configuration.

6.4.2.1 1 GMI configuration

We performed a wide range of gain to reach up to a gain product of 14718 for a high sensitivity value of about 72.6 V/mT.

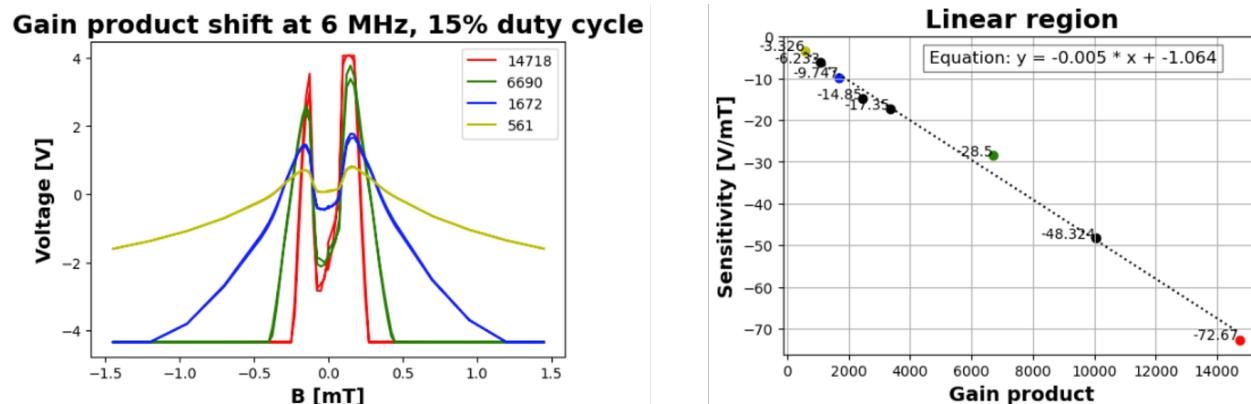


Figure 48: Red = 14718 Green = 6690 Blue = 1672 Yellow = 561 $G_{opa699} * G_{LT1920}$ gain shift

Similarly to the previous study we observe a linear behaviour of the sensitivity in what regard the evolution of the gain product.

6.4.2.2 2 GMI configuration

We then again perform in the same condition the gain shift for the dual GMI configuration.

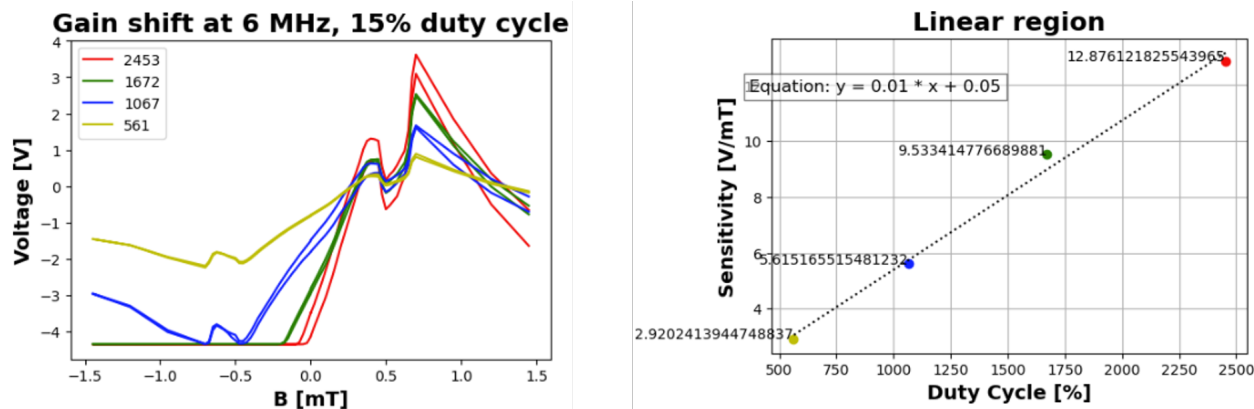


Figure 49: Red = 2453 Green = 1672 Blue = 1067 Yellow = 561 $G_{opa699} * G_{LT1920}$ gain shift

We can't go at higher value of gain product because of offset issue. Since we can't correct the offset in this configuration, at higher gain the curve where saturated. But at the same range of data the sensitivity is the same of around 0.01 [V/mT/Gain] for both configuration.

This conclude the study of the sensor using the Helmholtz coil setup.

6.5 Applicative test result using a kepco current supply

In this section, we will demonstrate the proper functionality of the current sensor by directly applying a current through the traces of the PCB. This injected current will be denoted as I_{PCB} , and we will observe its behavior during the testing process.

The schematic of the I_{PCB} injection toward the PCB is presented in (Figure 50). To further understand this phenomenon and the magnetic field induce by the I_{PCB} toward the GMI sample, we conducted a Python simulation to predict the expected magnetic field generated by the current trace on the sensitive GMI element depending on the distance between the two elements.

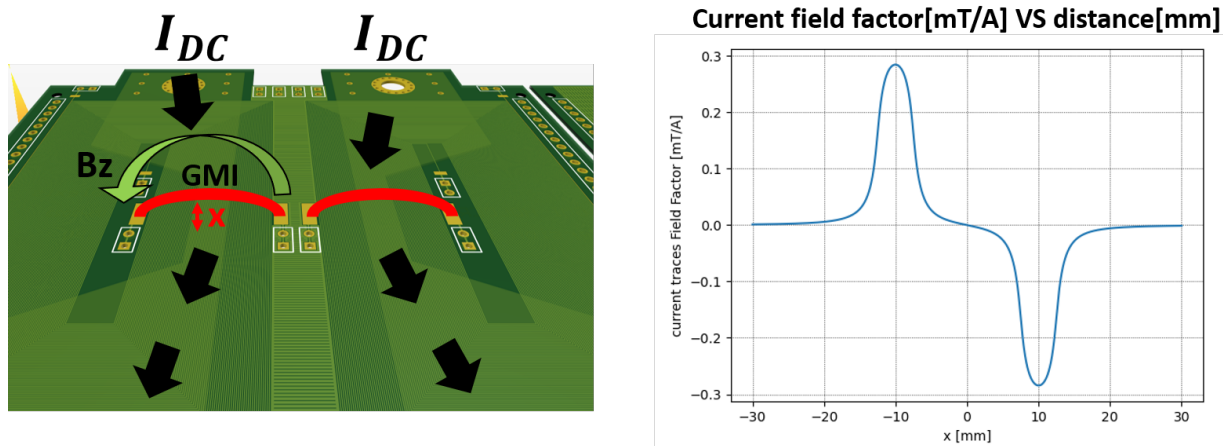


Figure 50: Current traces field factor

The next two paragraph are made to validate this model and the expected field factor of around 0.3 mT/A.

Indeed we will be injecting DC I_{PCB} current while biasing the PCB, and we will try to observe the linearity of the output around zero field apply.

6.5.1 1 GMI configuration

The test to effectively demonstrate and observe the device’s current detection capabilities was made in the same PCB configuration of Figure 44 (similar, gain, duty cycle, etc...).

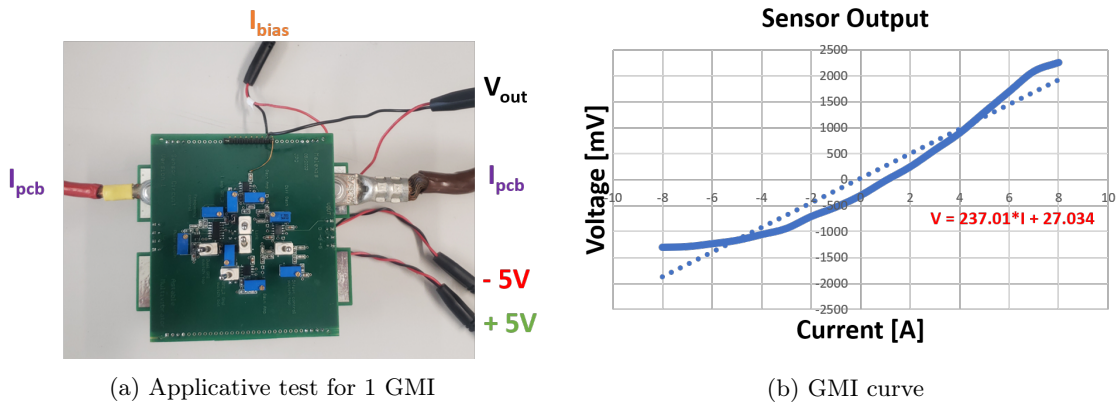


Figure 51: Linear output of the applicative test

The results from the current test with a PCB bias of 0.5 mT exhibit a linear DC current range of approximately 16 A, centered around 0 A. The sensitivity is measured to be around 237 mV/A, and should correspond to about 750 uT magnetic range. This yields a sensitivity of 5.056 V/mT, which is of a similar order of magnitude as the sensitivity observed in Figure 44. Furthermore the deduce field factor of the current traces is of about 0.047 mT/A which is 10 time lower than the simulation of Figure 50

We are now introducing an alternative current into the current traces of the PCB (I_{PCB}). This alternative current will operate at a frequency of 1 kHz and carry a 3.9 A rms current. Presented below are the sensor outputs in pink, showcasing both the biased and unbiased mode. In yellow the I_{PCB} current and in blue the voltage across the GMI sample.

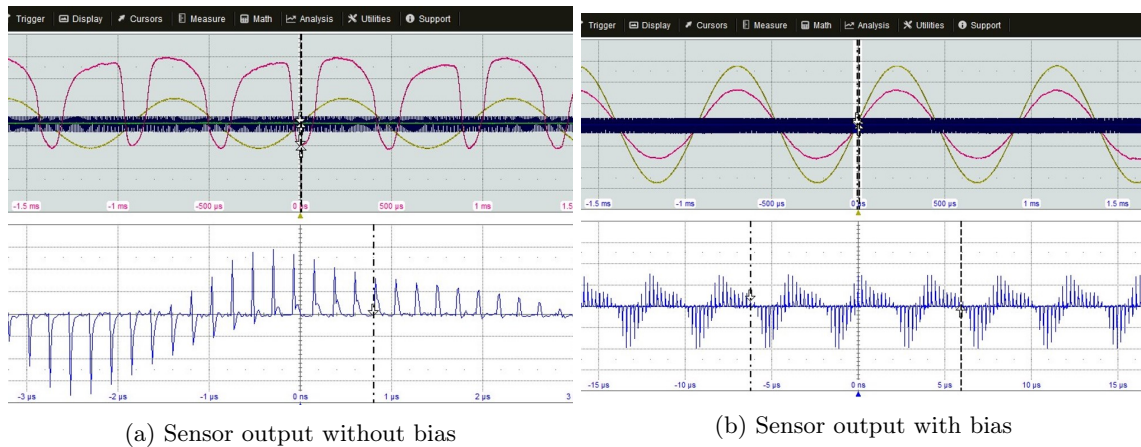


Figure 52: Yellow = Traces current, Pink = Sensor voltage output, Blue = GMI modulated voltage

As anticipated, when operating without bias, we observe the GMI impedance characteristic as depicted

in Figure 44. However, upon introducing bias, the output voltage impeccably tracks the variations of the current traces (see Figure 55b).

6.5.2 2 GMI configuration

For the 2 GMI configuration we configured the current traces in two modes which are the following:

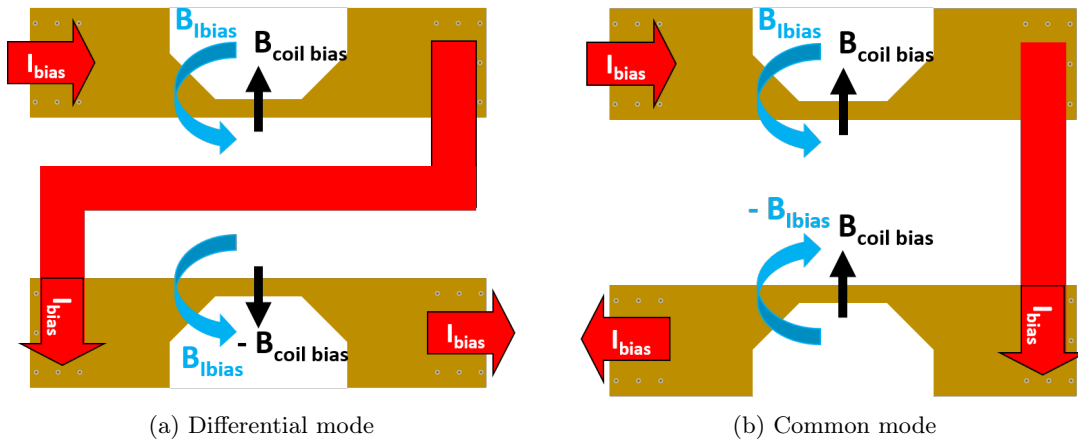


Figure 53: 2 GMI, current traces configuration

1. Differential mode: Opposite coil bias and a current bias which create the same magnetic field for both GMI
2. Common mode: Same coil bias but a biasing current that create opposite magnetic field for the GMI samples.

In the next step, we conducted an applicative test, similar to the one shown in Figure 51, with the following configuration: 6 MHz frequency, 10% duty cycle, 100 Ω injection resistance, $G_{opa699} = 20$, and $G_{LT1920} = 100$. It was essential to ensure that the gain was not too high to avoid saturation, as we did not incorporate an offset corrector in this mode during the design process.

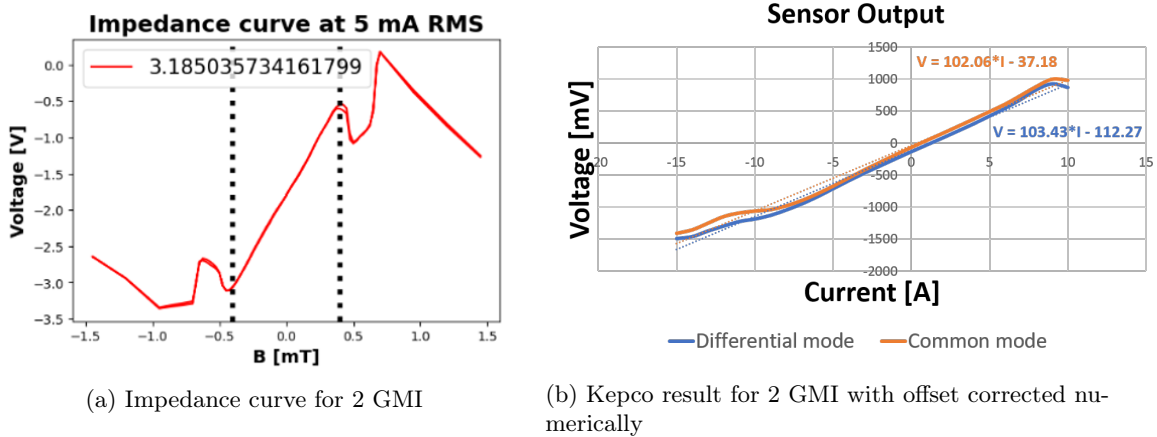


Figure 54: Linear output of the applicative test for 2 GMI

To begin with, the results for the differential and common mode showed remarkable similarity. The sensitivity achieved was around 102 mV/A, and the current range covered approximately 16 A in the more linear region. Notably, we observed a magnetic range of 800 uT on the left side, leading us to deduce a corresponding sensitivity of 2.04 V/mT, which closely aligns with the 3.18 V/mT displayed on the left side. We then introduce I_{PCB} as an alternating current of frequency 1kHz and amplitude of 5A. Here are the result of the sensor with and without bias:

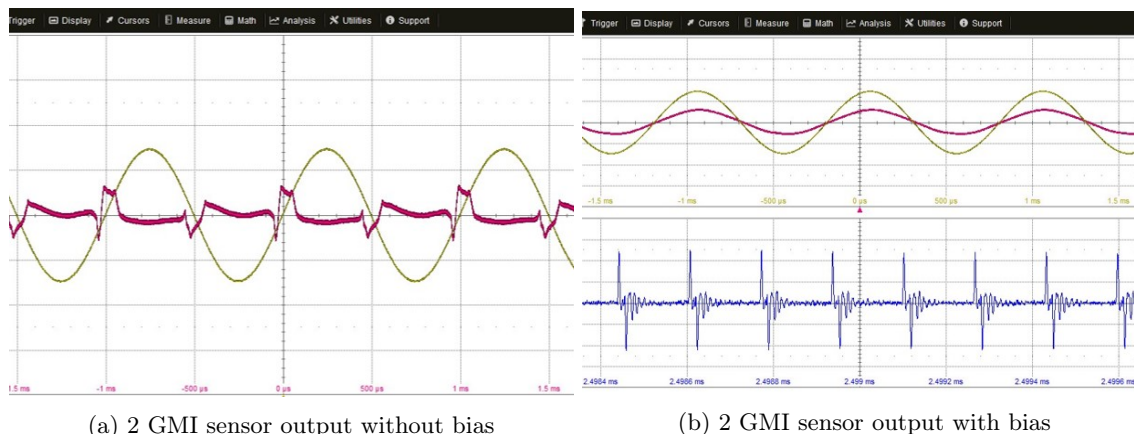


Figure 55: Yellow = Traces current, Pink = Sensor voltage output, Blue = GMI modulated voltage

The left curve emphasizes the asymmetry of the impedance curve between our two GMI samples. Had they been perfectly identical, we would have obtained a zero output in the non-biasing configuration. However, on the left side, when biased, the output sensor perfectly follows the input current.

6.6 Addressing drawbacks and exploring sensor amelioration

In this concluding chapter, we comprehensively examine the limitations of the sensor, encompassing aspects like bandwidth, noise, and numerous other factors. Understanding these limitations is vital for informed decision-making and accurate interpretation of results.

6.6.1 Bandwidth

One of the first thing we tested for the sensor was it’s bandwidth. Indeed we increased the frequency of I_{PCB} and observed the output of the sensor.

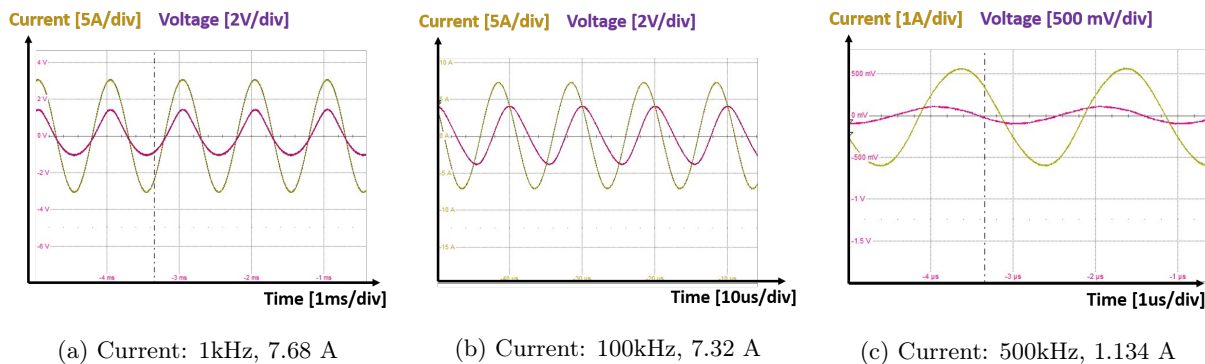


Figure 56: Current input and voltage output of the sensor for different frequencies

Presented above are various oscilloscope screenshots displaying the I_{PCB} taken at different frequencies in yellow and the corresponding sensor output in pink.

Subsequently, we generate the bode diagram illustrating the gain, the gain variation and phase shift against frequency, covering the range up to 100 kHz. Indeed after 500 kHz there was no signal to be seen at the output.

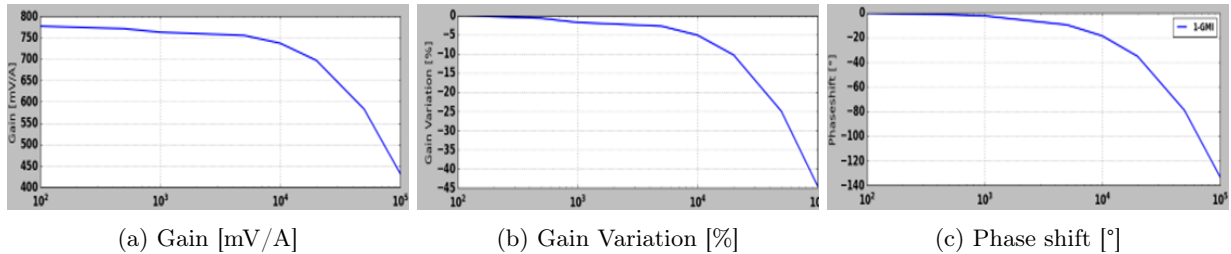


Figure 57: Bode diagramm study of the Voltage output over the Input I_{PCB} current

What we are observing is a change in slope for all three curves at approximately 10 kHz.

One possible reason for the lower-than-expected bandwidth is the phase shift induced by the current I_{PCB} and the magnetic field that it generate, as well as the limitations of the demodulation block to follow the detection of such high frequencies.

6.6.2 Noise

In this part we focused on trying to obtain a rough order of magnitude of the noise of the sensor in different configurations. Indeed, we maintained the RMS current entering inside the sensitive element at 10 mA RMS in all the test. Here is the protocol to obtain the noise of our system:

1. First we obtain the voltage RMS of the output of the excitation system when it's not connected to the GMI
2. Then we fixed the value of the injection resistance in order to have $V_{RMS}/R_{inj} = 10 \text{ mA}$
3. We extract the RMS value of the voltage output with and without I_{PCB} current. The last case correspond to the RMS noise

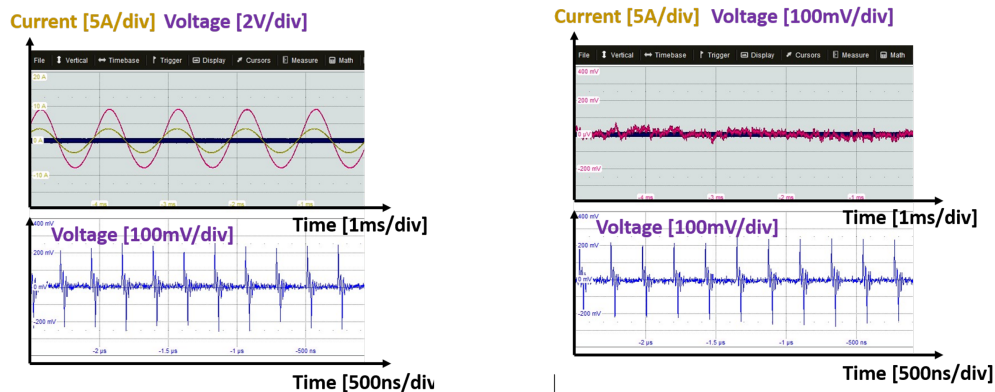


Figure 58: Voltage output with and without I_{PCB} current

4. We normalised our noise for a 2V pic to pic output for a range of $\pm 1.2\text{mT}$ application
5. Finally we calculate the free bit noise for a 500 Hz bandwidth application in order to compare with the specifications from [Figure 8](#)

Below, you'll find the graph on the right depicting the noise in free bits as a function of the duty cycle, comparing the PCB pulse and a commercial pulse with varying offset values. On the left side, there's a test involving a sinusoidal excitation system, showcasing the impact of increasing the amplitude and injection resistance.

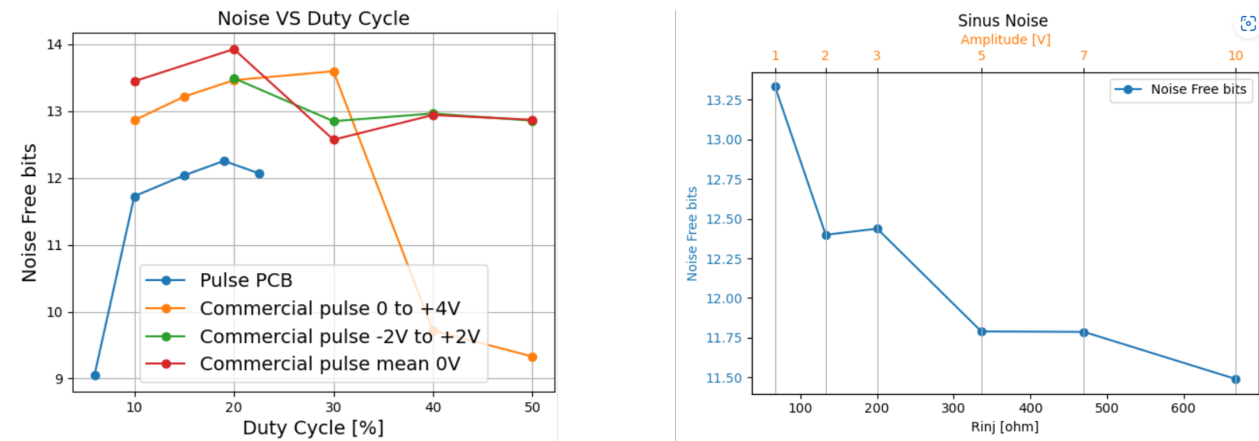


Figure 59: Voltage output with and without I_{PCB} current

In the context of digital signal processing, having a higher number of free bits indicates a lower level of noise. More free bits imply that the signal has a higher resolution and less quantization noise, resulting in more accurate representation and transmission of data.

The outcomes fall within the vicinity of the 12.5 free bit noise as outlined in the specifications. In fact, a majority of the excitation systems exhibit noise levels ranging from 12 to 14 free bits. The initial deduction is that the pulse on the PCB demonstrates higher noise levels compared to the commercial pulses, particularly when operating at the extremes of its capacity, such as a duty cycle of approximately 6%. Regarding the sinusoidal signal, both the augmentation of amplitude and the elevation of injection resistance contribute to an escalation in noise levels.

6.6.3 Some limitations

Other limitations where observe such as ringing as you can see with the voltage across the GMI:

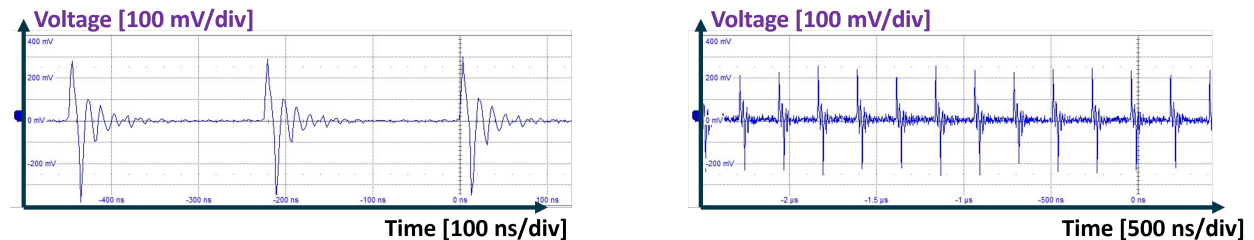


Figure 60: Ringing: 5% and 15% duty cycle

This ringing might be explained by the capacitive behavior inherent in the GMI sensitive element. This could give rise to a resonant circuit, potentially causing the observed ringing phenomenon.

Ultimately, there were areas in the sensor design that could be enhanced. For instance, the utilization of potentiometers proved imprecise and time-consuming for tuning. Moreover, the decision to integrate the entire PCB as a single unit caused challenges when attempting to replace the onboard excitation system with an external one. The pulse generated by the onboard PCB affected the signal even when not connected to the sensor.

7 Conclusion

In wrapping up my master's thesis, I have delved into the realm of highly sensitive current sensors through the utilization of the Giant Magneto Impedance (GMI) effect. With the guidance of Melexis' expertise in CMOS ferromagnetic layer deposition, I designed a GMI sensor incorporating essential components: excitation, demodulation, and amplification with offset correction. Employing extensive simulations via LTspice, I predicted the sensor's behavior and meticulously refine its design to achieve the desired outcomes.

A functional GMI current sensor was crafted on a PCB, capable of detecting fields ranging up to ± 400 μT using either one or two sensitive elements. The primary distinction observed between these two configurations was the requirement for an offset corrector. While the magnitudes of the detected fields were roughly comparable, the configuration employing two GMI elements exhibited superior linearity compared to the single-element counterpart under similar conditions. The applicative tests yielded conclusive results, affirming the sensor's capacity to accurately detect currents within the range of ± 10 A when properly biased.

Moreover, this sensor demonstrated the potential to achieve sensitivity up to 70 V/mT. When coupled with a feedback loop, this attribute opens the door to diverse applications. Throughout this thesis, I had the opportunity to gain proficiency in an array of software tools, including Altium, LTspice, and Python scripts for controlling measurement instruments. This experience has been invaluable in enriching my skill set and enhancing my understanding of sensor technology and its practical implementations.

In terms of comparing the reel project timeline with the [Figure 2](#), most of the steps took significantly more time than expected. Especially noteworthy are the prolonged durations for the LTspice simulation and the PCB design, which caused delays and resulted in a shortage of time for the characterization phase.

In conclusion, my journey through this thesis has been a rewarding one, offering insights into the intricate world of current sensor development and providing me with the tools to navigate it effectively.

8 ANNEX

8.1 List of figures

List of Figures

1	Internship locations	1
2	Estimated Gantt chart	2
3	GMI representation for a wire sample with the typical physical quantities involved	3
4	Skin effect: Current density at different frequencies through a wire	4
5	General impedance characteristic	5
6	Example of a biased curve for a longitudinal GMI anisotropy	5
7	Differential transducer characteristic for a longitudinal impedance curve	6
8	Melexis target specification	7
9	GMI sensor block diagram	7
10	Impedance variation according to magnetic field and frequency	8
11	Vitrovac 6030 impedance curve at $F = 9.11$ MHz	9
12	Block diagram of the two excitation GMI family	9
13	Exhaustive design of some oscillators	10
14	Design of some GMI integrated oscillators	11
15	Amplitude demodulation explained in term of frequency, $F_{carrier} = AC$ current frequency, $F_{modulated} = External$ magnetic field frequency	12
16	Exhaustive list of demodulation systems	13
17	Chosen GMI sensor block diagram	14
18	Overall sensor with one GMI	15
19	Entire Excitation system	15
20	Spice curve of RC astable multivibrator	16
21	Spice curve of the pulse width modulator	17
22	Spice curve of the output of the buffer	17
23	GMI spice model, GMI voltage, GMI impedance for different magnetic field	18
24	Spice Demodulation Block	19
25	Limiting amplifier rectifying curve	19
26	Low pass filter spice curve	20
27	Offset and amplification block	21
28	Final block output	21
29	Some calibration steps	22
30	Sensor range output for different GMI value	23
31	LTspice noise study	24
32	Overall sensor with two GMI	25
33	Dual astable oscillator	25
34	Voltage at the GMI samples	26
35	Dual GMI Sensor range output for different GMI combination	26
36	Noise for a dual GMI configuration	27
37	Biasing coil design	28
38	Altium GMI holder PCB	29
39	Altium electronics PCB	30
40	Final sensor PCB	31
41	3D printed pieces	32
42	Biasing coil measurement across the GMI	32
43	Helmholtz setup	33
44	Impedance characteristic, linear domain, and absolute deviation at 6 MHz, 5% duty cycle	34

45	Impedance characteristic for different opposing current Green = 50 mA, Red = 200 mA - $G_{opa699} = 11$, $G_{LT1920} = 100$, 6 Mhz pulse and 15% duty cycle	34
46	Red = 20% Green = 15% Blue = 10% Yellow = 5% duty cycle	35
47	Red = 18.5% Green = 15% Blue = 10% Yellow = 5% duty cycle	36
48	Red = 14718 Green = 6690 Blue = 1672 Yellow = 561 $G_{opa699} * G_{LT1920}$ gain shift	36
49	Red = 2453 Green = 1672 Blue = 1067 Yellow = 561 $G_{opa699} * G_{LT1920}$ gain shift	37
50	Current traces field factor	37
51	Linear output of the applicative test	38
52	Yellow = Traces current, Pink = Sensor voltage output, Blue = GMI modulated voltage	38
53	2 GMI, current traces configuration	39
54	Linear output of the applicative test for 2 GMI	39
55	Yellow = Traces current, Pink = Sensor voltage output, Blue = GMI modulated voltage	40
56	Current input and voltage output of the sensor for different frequencies	40
57	Bode diagramm study of the Voltage output over the Input I_{PCB} current	41
58	Voltage output with and without I_{PCB} current	41
59	Voltage output with and without I_{PCB} current	42
60	Ringings: 5% and 15% duty cycle	42
61	3D Helmholtz coil measurement setup	46
62	Dual integrated GMI oscillator	47
63	Output of the integrated oscillator	48
64	Inverter Model: 74HC14D Nexperia: ANALOG MODEL	49
65	Limiting amplifier Model: OPA699	49
66	Transistor Model: ALDXX	50

8.2 References

References

- [1] E. P. Harrison, G. L. Turney, H. Rowe, and H. Gollop. "The Electrical Properties of High Permeability Wires Carrying Alternating Current". In: *Proc. R. Soc. Lond. Ser. Math. Phys. Sci.* 157.891 (1936), pp. 451–479 (cit. on p. 3).
- [2] L. V. Panina and K. Mohri. "Magneto-impedance effect in amorphous wires". In: *Applied Physics Letters* 65.9 (Aug. 1994), pp. 1189–1191 (cit. on p. 3).
- [3] J. Nabias. "Capteur de Courant à Magnéto-Impédance Géante (GMI) souple et portatif". PhD thesis. theses, 2018. URL: <https://theses.hal.science/tel-01863989> (cit. on pp. 3, 6).
- [4] P.S. Traore. "Introduction des techniques numériques pour les capteurs magnétiques GMI (giant magneto-impedance) à haute sensibilité: Mise en œuvre et performances". PhD thesis. theses, 2018. URL: <https://theses.hal.science/tel-01720331> (cit. on p. 4).
- [5] LEM. "Capteurs isolés de courant et de tension caractéristiques - applications - calculs". In: (2017). URL: https://www.lem.com/images/stories/files/Products/P1_5_1_industry/CH24101F.pdf (cit. on p. 6).
- [6] M. Zidi. "Utilisation de la Magnéto-impédance géante pour la réalisation d'un capteur de Courant". PhD thesis. theses, 2015. URL: <https://theses.hal.science/tel-01133623> (cit. on p. 7).
- [7] T. Kanno, K. Mohri, T. Yagi, T. Uchiyama, and L. P. Shen. *Amorphous wire mi micro sensor using C-MOS IC multivibrator*. Available at: <https://ieeexplore.ieee.org/document/617943/>. Accessed: 03 August 2023. 1997 (cit. on p. 10).

8.3 Quick explanation of the measurement setup

The characterization setup primarily consists of a 3D Helmholtz coil system capable of generating magnetic fields along all three axes. This configuration allows for compensation of the Earth’s magnetic field, aided by a 3D magnetometer for field calibration. The intensity of these magnetic fields is precisely controlled using various current sources, which are operated through Python programming. The impedance of the sample is measured using a network analyzer, and the resulting data is exported to Excel for further analysis.

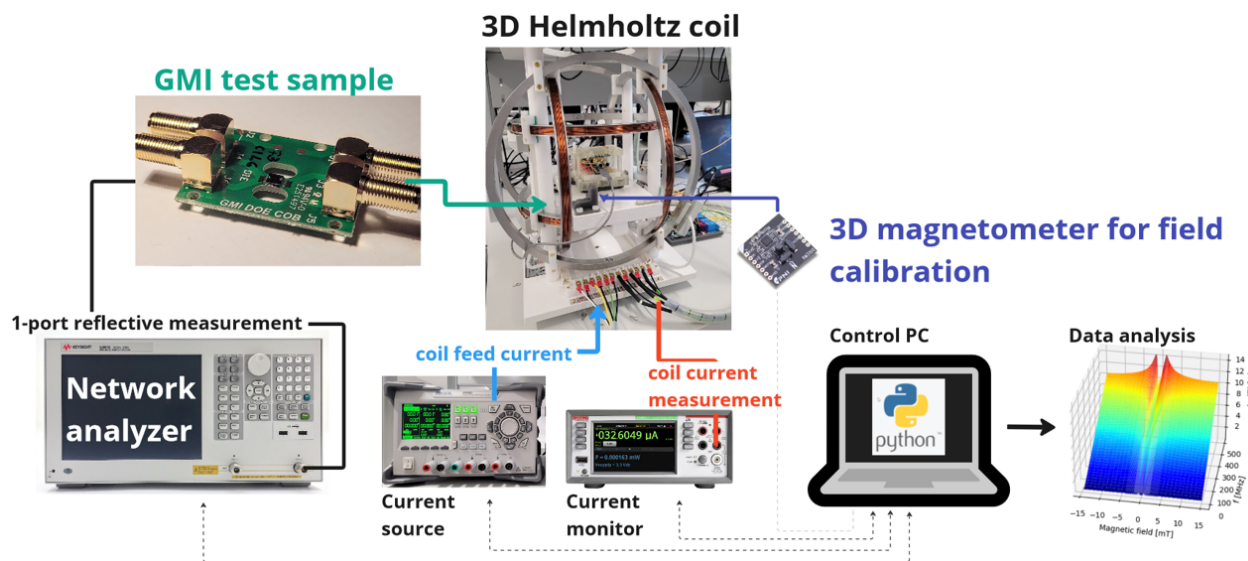


Figure 61: 3D Helmholtz coil measurement setup

The characterization setup mentioned will be utilized at a later stage in the project to effectively characterize the sensor demonstrator.

8.4 Voltage control oscillator

During this internship another type of oscillator has been simulated in order to have a first idea of the realisation of an integrated MOSFET dual GMI based oscillator. This oscillator will not be build during this internship. The following voltage control oscillator is a type of oscillator that is mainly used for radiofrequency application, generally at the order of magnitude of hundred of megahertz and even up to gigahertz. The frequency is generally tuned using a varycap but in our case the frequency and amplitude will be tuned by the variation of impedance of the two GMI. The resonant circuit utilized in the design incorporates the ALD1101 NMOS transistor model, while the current source employs the ALD1102 PMOS matched transistor model. These specific transistor models, which are crucial components of the circuit, have been employed for their desired characteristics and performance. The detailed specifications and parameters of these models can be found at the end of this report, providing comprehensive information for further analysis and understanding of their behavior within the circuit:

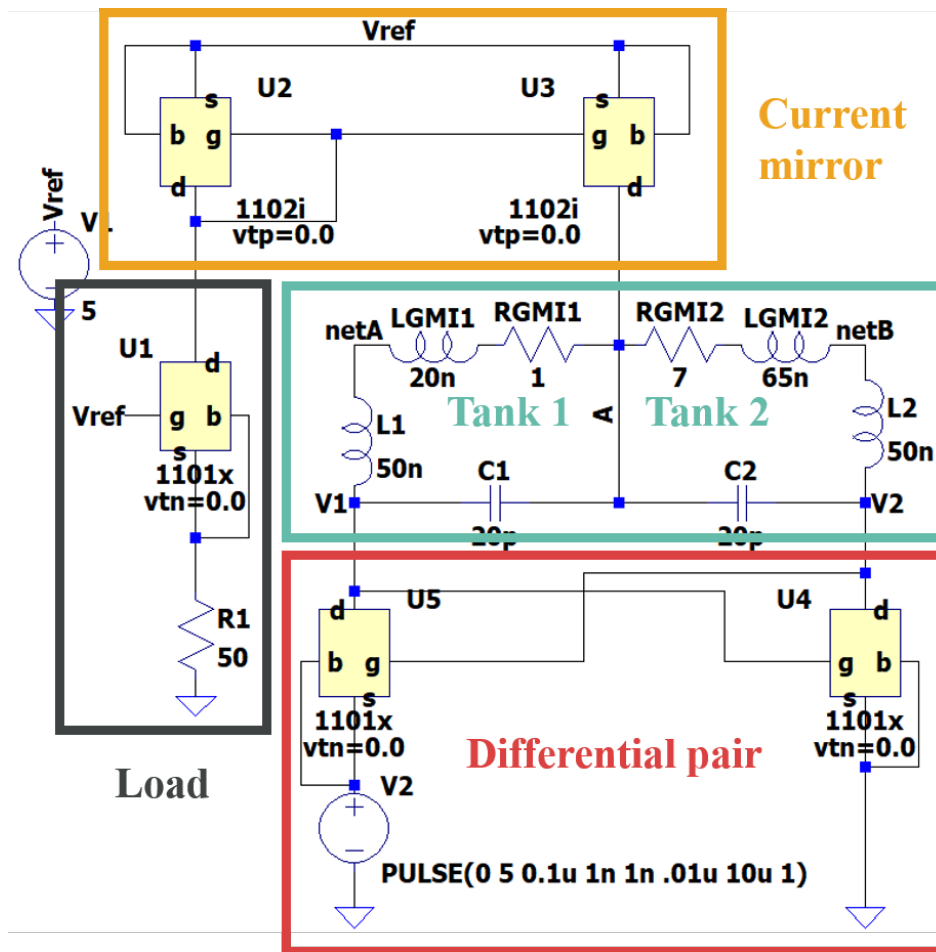


Figure 62: Dual integrated GMI oscillator

The oscillator architecture consists of a differential pair configuration that is cross-coupled to create positive feedback (U5, U4). Each transistor in the differential pair has its input connected to the output of the opposite transistor. The differential output signal, represented by $V_o = V_1 - V_2$, is obtained from the voltage difference between the outputs of the two transistors.

Each transistor in the pair acts as a common-source amplifier, featuring a complex load comprising a parallel

combination of the GMI (inductor + resistor) and a capacitor. This load, often referred to as a "tank" circuit, effectively stores oscillating energy to fix the output frequency. It plays a critical role in sustaining the oscillations.

To ensure proper operation, a well-designed active current source is required to provide DC biasing to node 'A', which in turn biases transistors U4 and U5. Additionally, the active current source needs to maintain a high AC impedance between node 'A' and the supply rail. This high impedance is crucial in preventing RF energy from "leaking" out of the tank circuits and interfering with the oscillations by dissipating into the supply rail.

You will find below some curve result of the sinusoidal output for different combination value for the two GMI sample:

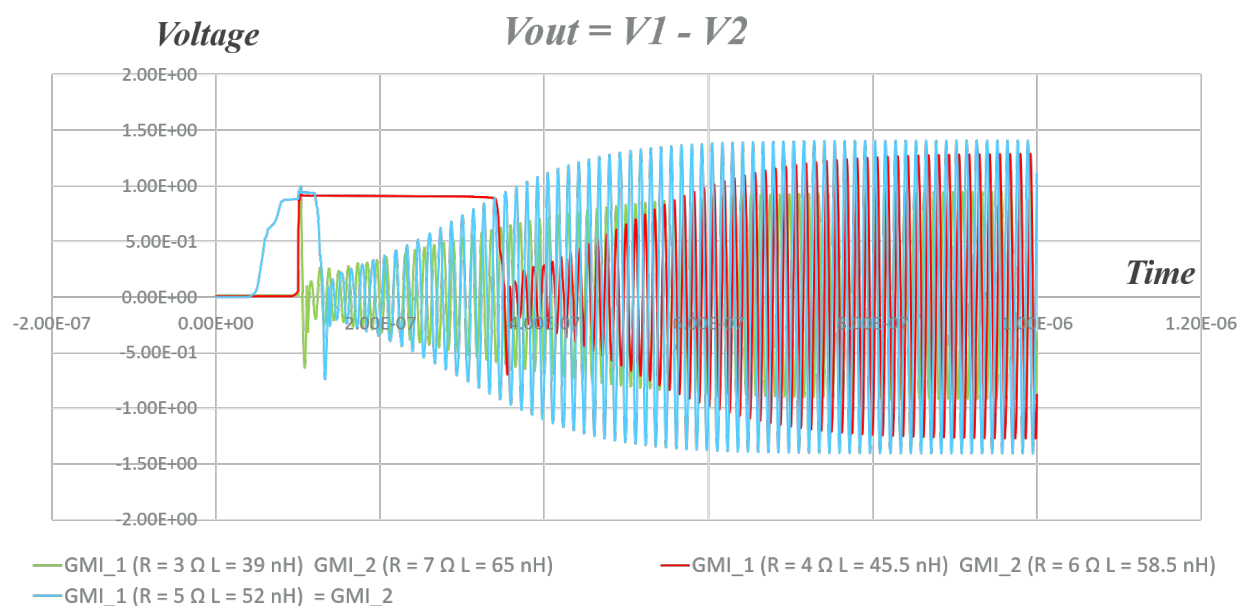


Figure 63: Output of the integrated oscillator

Upon observation, it is evident that there is an amplitude variation that can reach up to 500 mV. However, due to the higher operating frequency of approximately 85 MHz, accurately assessing frequency changes in LTspice becomes more challenging as the variations occur on the order of hundreds of kilohertz. The precision required to capture these frequency changes at such high frequencies poses a difficulty in accurately simulating the behavior in LTspice.

8.5 Complementary figures and tables

```
.Model MHC PEN PMOS
+LEVEL = 3
+KP = 22.1E-6
+VTO = -0.71
+TOX = 51.5E-9
+NSUB = 3.3E16
+GAMMA = 0.92
+PHI = 0.65
+VMAX = 970E3
+RS = 80
+RD = 80
+XJ = 0.63E-6
+LD = 0.23E-6
+DELTA = 2.24
+THETA = 0.108
+ETA = 0.322
+KAPPA = 0.0
+WD = 0.0
```

```
.Model MHC NEN NMOS
+LEVEL = 3
+KP = 45.3E-6
+VTO = 0.72
+TOX = 51.5E-9
+NSUB = 2.8E15
+GAMMA = 0.94
+PHI = 0.65
+VMAX = 150E3
+RS = 40
+RD = 40
+XJ = 0.11E-6
+LD = 0.52E-6
+DELTA = 0.315
+THETA = 0.054
+ETA = 0.025
+KAPPA = 0.0
+WD = 0.0
```

```
.SUBCKT SMTIN 2 3 50 60
* SCHMITT-TRIGGER INPUT FOR HCl4 CMOS INPUT LEVELS
*IN=2, OUT=3, VCC=50, GND=60
R1 2 4 100
MP1 4 50 50 MHC PEN W=200 L=2.4U AD=100P AS=100P PD=40U PS=20U
MN1 4 60 60 MHC NEN W=350 L=2.4U AD=140P AS=140P PD=50U PS=35U
MP2 5 4 50 50 MHC PEN W=360 L=2.4U AD=140P AS=140P PD=50U PS=35U
MN2 6 4 60 60 MHC NEN W=160 L=2.4U AD= 70P AS= 70P PD=15U PS=17U
MP3 3 4 5 50 MHC PEN W=44U L=2.4U AD=220P AS=220P PD=60U PS=44U
MN3 3 4 6 6 MHC NEN W=17U L=2.4U AD= 70P AS= 70P PD=15U PS=16U
MP4 5 3 60 50 MHC PEN W=360 L=2.4U AD=150P AS=150P PD=60U PS=36U
MN4 6 3 50 6 MHC NEN W= 6U L= 4U AD= 25P AS= 25P PD=10U PS= 6U
.ENDS

.SUBCKT INVN 2 3 50 60
*IN=2, OUT=3, VCC=50, GND=60
MP1 3 2 50 50 MHC PEN W=364U L=2.4U AD=500P AS=500P PD=10U PS=430U
MN1 3 2 60 60 MHC NEN W=184U L=2.4U AD=275P AS=275P PD=10U PS=270U
.ENDS

.SUBCKT OUTPN 2 3 50 60
*IN=2, OUT=3, VCC=50, GND=60
R1 2 4 100
MP1 3 4 50 50 MHC PEN W=360U L=2.4U AD=400P AS=400P PD=10U PS=180U
MN1 3 4 60 60 MHC NEN W=140U L=2.4U AD=200P AS=300P PD=10U PS=130U
R2 4 5 50
MP2 3 5 50 50 MHC PEN W=360U L=2.4U AD=400P AS=400P PD=10U PS=180U
MN2 3 5 60 60 MHC NEN W=140U L=2.4U AD=200P AS=200P PD=10U PS=130U
R3 5 6 50
MP3 3 6 50 50 MHC PEN W=360U L=2.4U AD=400P AS=400P PD=10U PS=180U
MN3 3 6 60 60 MHC NEN W=140U L=2.4U AD=200P AS=200P PD=10U PS=130U
.ENDS

.SUBCKT 74HC14D Nexperia 20 30 80 90
*.SUBCKT INVSMT 20 30 80 90
*IN=20, OUT=30, VCC=90, GND=90
XINP 20 25 80 90 SMTIN
XINV 25 35 80 90 INVN
XOUTP 35 30 80 90 OUTPN
.ENDS
```

Figure 64: Inverter Model: 74HC14D Nexperia: ANALOG MODEL

```
.MODEL NPN8 NPN
+ IS = 7.604E-18 BF = 1.570E+02 NF = 1.000E+00 VAF= 7.871E+01
+ IKF= 3.975E-02 ISE= 3.219E-14 NE = 2.000E+00 BR = 7.614E-01
+ NR = 1.000E+00 VAR= 1.452E+00 IKR= 8.172E-02 ISC= 7.618E-21
+ NC = 1.847E+00 RB = 1.060E+02 IRB= 0.000E+00 RBM= 2.400E+00
+ RE = 2.520E+00 RC = 1.270E+02 CJE= 1.120E-15 VJE= 7.591E-01
+ MJE= 5.406E-01 TF = 1.213E-11 XTF= 2.049E+00 VTF= 1.813E+00
+ ITF= 4.293E-02 PTF= 0.000E+00 CJC= 8.208E-14 VJC= 6.666E-01
+ MJC= 4.509E-01 XCJC=8.450E-02 TR = 4.000E-11 CJS= 1.160E-15
+ VJS= 5.286E-01 MJS= 4.389E-01 XTB= 1.022E+00 EG = 1.120E+00
+ XTI= 1.780E+00 KF = 3.500E-16 AF = 1.000E+00 FC = 8.273E-01
*
.MODEL PNP8 PNP
+ IS = 7.999E-18 BF = 1.418E+02 NF = 1.000E+00 VAF= 4.158E+01
+ IKF= 1.085E-01 ISE= 2.233E-15 NE = 1.505E+00 BR = 3.252E+01
+ NR = 1.050E+00 VAR= 1.093E+00 IKR= 5.000E-05 ISC= 6.621E-16
+ NC = 1.150E+00 RB = 6.246E+01 IRB= 0.000E+00 RBM= 2.240E+00
+ RE = 2.537E+00 RC = 1.260E+02 CJE= 9.502E-14 VJE= 7.320E-01
+ MJE= 4.930E-01 TF = 1.303E-11 XTF= 3.500E+01 VTF= 3.259E+00
+ ITF= 2.639E-01 PTF= 0.000E+00 CJC= 1.080E-13 VJC= 7.743E-01
+ MJC= 5.000E-01 XCJC=8.504E-02 TR = 1.500E-10 CJS= 1.290E-13
+ VJS= 9.058E-01 MJS= 4.931E-01 XTB= 1.732E+00 EG = 1.120E+00
+ XTI= 2.000E+00 KF = 3.500E-16 AF = 1.000E+00 FC = 8.500E-01

.SUBCKT OPA699 + - V+ V- Out VBI VIO
D.D1 17 14 DI 1
D.D3 19 20 DI 1
D.D4 20 21 DI 1
R.R3 17 19 500
R.R4 18 21 500
R.R5 19 23 420
R.R2 16 16 420
R.D2 14 18 DI 1
R.R1 12 14 420
R.R5 22 14 420
D.D42 34 33 DI 1
D.D43 35 34 DI 1
E.E5 34 0 VALUE LIM(V(32),V(VLO)-10m,V(VHI)+10m)
G.G12 0 32 NCMP 0 1m
Q.Q2 0 - 11 NPN8 .333
Q.Q1 0 - 10 PNP8 .333
R.R8 24 14 420
R.R7 19 29 420
I.I7 27 14 DC 230u
I.I8 11 14 DC 230u
I.I9 17 17 DC 480u
I.I2 11 14 DC 230u
I.I3 19 19 DC 480u
I.I4 18 18 DC 480u
I.I6 21 14 DC 480u
I.I9 19 19 DC 2.5m
I.I10 37 14 DC 5.5m
V.V1 35 33 DC 1.35
V.V2 13 13 DC 1.35
Q.Q3 13 10 14 PNP8 .667
Q.Q4 13 10 14 NPN8 .333
Q.Q5 15 11 14 PNP8 .333
Q.Q6 15 15 16 PNP8 .667
Q.Q7 20 13 22 PNP8 .667
Q.Q8 20 15 23 PNP8 .667
Q.Q9 25 25 24 PNP8 .667
Q.Q10 25 26 20 NPN8 .333
Q.Q11 28 27 20 PNP8 .333
Q.Q12 28 28 29 NPN8 .667
Q.Q13 14 14 DC 230u
Q.Q14 14 14 DC 230u
Q.Q15 NCMP 25 30 PNP8 .667
Q.Q16 NCMP 28 31 NPN8 .667
Q.Q17 14 14 DC 230u
Q.Q18 14 14 DC 230u
Q.Q19 38 36 39 PNP8 29
Q.Q20 40 37 39 PNP8 29
R.R9 30 14 420
R.R10 14 31 420
R.R11 0 32 1k
R.R12 38 14 35
R.R13 14 14 DC 20
C.C1 NCMP 14 450f
C.C2 32 0 500f
C.C3 0 Out 750f
C.C4 0 + 750f
C.C5 0 - 750f
.ENDS OPA699
```

Figure 65: Limiting amplifier Model: OPA699

```

.model nca nmos (Level=2
+   gamma=1.09 lot/4/uniform=-.22 dev/uniform=.01
+   vto=(.75+vtn) lot/2/uniform=.2 dev/uniform=1e-3
+   Uo=650 lot/3/uniform=40 dev/uniform=.5
+   Ucrit=0.7e4 Uexp=.1 Vmax=1.6e5
+   phi=.70 tpg=+1
+   nsub=(1e16*ires) neff=(10*ires) nss=.7e11 nfs=1.17e11
+   tox=(.055u*cox) lot/8/uniform=9.1% dev/uniform=.05%
+   Cgso=(.94n*cox) Cgdo=(.59n*cox) Cgbo=(.138n*pox) Xqc=.42
+   cj=.39m mj=.5 cjsw=264p mjsw=0.18
+   xj=2.0u
+   ld=1.6u lot/uniform=.19u dev/uniform=.15u
+   wd=1.05u lot/uniform=.41u dev/uniform=.1u
+   pb=.9 js=20.u lot/uniform=50% dev/uniform=80%
+   jssw=2.07e-10 lot/uniform=50% dev/uniform=80%
+   kf=.75e-28 rsh=10 lot/1/uniform=4 dev/uniform=.5)
+
.model pca pmos (level=2
+   vto=(-.74+vtp) lot/5/uniform=.2 dev/uniform=1e-3
+   gamma=.58 lot/7/uniform=.2 dev/uniform=.01
+   Uo=260 lot/6/uniform=20 dev/uniform=.6
+   Ucrit=1.0e4 Uexp=.16 Vmax=3.0e5
+   phi=.70 tpg=-1
+   nsub=1e16 Neff=1 nss=1e11 nfs=1.06e11
+   tox=(.055u*cox) lot/8/uniform=9.1% dev/uniform=.05%
+   Cgso=(.61n*cox) Cgdo=(.39n*cox) Cgbo=.138n Xqc=.42
+   cj=.18m cjsw=322p
+   xj=1.2u ld=.96u wd=.5u pb=.9 mj=.57 mjsw=0.33
+   js=20e-6 lot/uniform=50% dev/uniform=80%
+   jssw=2.07e-10 lot/uniform=50% dev/uniform=80%
+   kf=.75e-28 rsh=90 lot/9/uniform=20 dev/uniform=4)
+
.subckt l101x 1 2 3 4 params: vtn=0.0
m1 1 2 3 4 nca l=7.8e-6 w=1.106e-3 as=4.825e-8 ps=3.82e-3 ad=1.286e-8
+   nrd=.3 nrs=1 nrg=25 nrb=35
.ends

.subckt l102i 1 2 3 4 params: vtp=0.0
* (a five terminal device does not exist.)
mt 1 2 3 4 pca l=7.8e-6 w=1.106e-3 as=4.825e-8 ps=3.82e-6 ad=1.286e-8
+   nrd=.3 nrs=1 nrg=25 nrb=35
.ends

```

Figure 66: Transistor Model: ALDXX